Available online at www.sciencedirect.com
ScienceDirect
Journal of Power Sources 166 (2007) 1–21
JOURNAL OF POWER SOURCES
www.elsevier.com/locate/jpowsour

A transient PEMFC model with CO poisoning and mitigation by O_2 bleeding and Ru-containing catalyst

A.A. Shah [a,*], P.C. Sui [b], G.-S. Kim [c], S. Ye [c]

[a] *Queen's, RMC Fuel Cell Research Centre, 945 Princess Street, Kingston, Ont. K7L 5L9, Canada*
[b] *Institute for Integrated Energy Systems, University of Victoria, Victoria, BC V8W 3P6, Canada*
[c] *Ballard Power Systems, 4343 North Fraser Way, Burnaby, BC V5J 5J9, Canada*

Received 5 December 2006; received in revised form 31 December 2006; accepted 2 January 2007
Available online 17 January 2007

Abstract

In this paper we present a transient, fully two-phase, non-isothermal model of carbon monoxide poisoning and oxygen bleeding in the membrane electrode assembly of a polymer electrolyte fuel cell. The model includes a detailed description of mass, heat and charge transport, chemisorption, electrochemical oxidation and heterogeneous catalysis (when oxygen is introduced). Example simulation results demonstrate the ability of the model to qualitatively capture the fundamental features of the poisoning process and the extent of poisoning with respect to channel temperature and concentration. Further examples show how the multi-step kinetics can interact with other physical phenomena such as liquid-water flooding, particularly in the anode. Carbon monoxide pulsing is simulated to demonstrate that the complicated reaction kinetics of oxygen bleeding can be captured and even predicted. It is shown that variations in the channel temperature have a convoluted effect on bleeding, and that trends in performance on relatively short time scales can be the precise opposite of the trends observed at steady state. We incorporate a bi-functional mechanism for carbon monoxide oxidation on platinum–ruthenium catalysts, demonstrating the marked reduction in the extent of poisoning, the effect of variations in the platinum–ruthenium ratio and the influence of temperature. Finally, we discuss the implications of the results, extensions to the model and possible avenues for experimental work.

Keywords: Transient model; Two-phase; CO poisoning; Oxygen bleeding; Platinum–ruthenium

1. Introduction

The proton exchange membrane fuel cell (PEMFC) is an emerging source of clean and efficient energy, particularly for application in the automotive industry. In a basic description of the PEMFC hydrogen (H_2) is electro-oxidated at the anode producing protons and electrons, with simultaneous oxygen (O_2) reduction at the cathode from the protons migrating through the membrane and the electrons entering through an external circuit. The net product is simply water. The reactants are delivered through a carbon paper, known as the gas diffusion layer (GDL), and reaction takes place in catalyst layers (CL) on either of the membrane—the catalyst in question being platinum (Pt). The unit comprising GDL, CL and membrane is termed the membrane electrode assembly (MEA).

However, there are several factors that complicate a practical implementation, notably flooding of the CL (restricted ingress of reactants), membrane drying (decreased protonic conductivity), inefficient use of the Pt (reaction can only occur at points of contact between the Pt, carbon and electrolyte) and degradation, through, for example, radical attack of the membrane, carbon monoxide (CO) poisoning, Pt dissolution and carbon corrosion. These factors are in turn influenced by the properties of the several components of the cell and the conditions under which the cell is operated, for example relative humidity, temperature and fuel composition. In order for the protons generated at the anode to reach the cathode freely the membrane must remain well hydrated. The GDL must facilitate efficient delivery of the reactants from the channels to the CL, but, at the same time, must be sufficiently hydrophobic to expel any build-up of liquid-water, without compromising the hydration level of the membrane. These issues are a selection of those that have formed the focus of modelling studies of PEMFC. The

* Corresponding author. Tel.: +1 778 288 4292; fax: +1 604 268 6657.
E-mail address: ashah@pims.math.ca (A.A. Shah).

0378-7753/$ – see front matter © 2007 Published by Elsevier B.V.
doi:10.1016/j.jpowsour.2007.01.020

Nomenclature

a	specific surface area of Pt (m^{-1})
a_w	water activity
A	specific surface area of agglomerates (m^{-1})
b_{ads}	desorption coefficient ($mol\,m^{-3}$)
C	molar concentration or specific heat capacity ($mol\,m^{-3}$or $J\,kg^{-1}\,K^{-1}$)
d	mean pore diameter (m)
D	diffusion coefficient ($m^2\,s^{-1}$)
E_{ads}	activation energy (adsorption) ($J\,mol^{-1}$)
E_{ox}	activation energy (oxidation) ($J\,mol^{-1}$)
E_0	open circuit voltage (V)
F	Faraday's constant ($C\,mol^{-1}$)
h	mass transfer coefficient (s^{-1})
H	Henry's constant or Heaviside function
i	exchange current density ($A\,m^{-2}$)
$\mathcal{J}$	Leverette function
k	thermal conductivity ($W\,m^{-1}\,K^{-1}$)
k_{ads}	adsorption coefficient ($m\,s^{-1}$)
k_{ox}	electro-chemical oxidation rate ($mol\,m^{-2}\,s^{-1}$)
L	thickness (m or μm)
m	loading ($kg\,m^{-2}$)
N	agglomerate density (m^{-3})
p	liquid pressure (Pa)
P	gas pressure (Pa)
q	surface reaction rate ($mol\,m^{-2}\,s^{-1}$)
r	interaction parameter ($J\,mol^{-1}$)
R	universal gas constant ($J\,mol^{-1}\,K^{-1}$)
R_a	agglomerate radius (m)
$\mathcal{R}_O$	ORR rate ($mol\,m^{-3}\,s^{-1}$)
s	saturation
S	source/sink ($mol\,m^{-3}\,s^{-1}$ or $W\,m^{-3}$ or $A\,m^{-3}$)
t	time (s)
T	temperature (K)
v	velocity ($m\,s^{-1}$)
V_{cell}	cell voltage (V)
W	molar mass ($kg\,mol^{-1}$)
x	distance (m or μm)
X	molar fraction

Greek letters

α	transfer coefficient
β	symmetry factor
γ	diffusion rate through films (s^{-1})
δ	film thickness (m or μm)
Δ	entropy ($J\,mol^{-1}\,K^{-1}$)
ϵ	volume fraction
η	overpotential (V)
θ	contact angle or surface coverage (° or −)
κ	absolute permeability (m^2)
κ_a and κ_d	adsorption and desorption coefficients ($m\,s^{-1}$)
λ	membrane water content
μ	dynamic viscosity ($kg\,m^{-1}s^{-1}$)
ν	fixed charge site concentration ($mol\,m^{-3}$)
ρ	density or molar area density ($kg\,m^{-3}$ $kg\,m^{-2}$)
σ	conductivity ($S\,m^{-1}$)
σ'	surface tension ($N\,m^{-1}$)
ϕ	potential (V)
Ω	water removal constant (m^{-1})

Subscripts

a	agglomerate or anode or adsorption
ads	adsorption
b	backward (reaction)
c	cathode or capillary or CCL or condensation
CO	CO
d	dissolved or desorption
e	electrolyte
g	GDL or gas
H	H_2
k	forward (rate constants)
l	liquid
M	free site (Pt/Ru)
N	N_2
ox	oxidation
O	O_2
p	pore space
pt	platinum
r	reaction
ref	reference
Ru	ruthenium
s	solid or electronic
T	total value
v	vapour
w	water
0	reference

Superscripts

c	CCL
CO	CO
CO– O	CO oxidation
f	film
g	GDL
H	H_2
H– O	H_2 oxidation
O	O_2
s	surface
*	equilibrium value
–	boundary/initial value

vast majority of models are steady-state, despite the obvious transient nature of cell operation (performance) in automobile applications. Degradation phenomena are also transient, impacting performance on a long time scale, such as carbon corrosion and Pt dissolution, or on a relatively short time scale, such as CO poisoning. Moreover, several other critical issues, notably freeze–start and startup–shutdown, are strictly transient.

Given its impact, water management, particularly of the liquid form, has received a great deal of attention, [1–9].

Simplifying assumptions are regularly adopted because of the complexity of the system, such as one or more of: regularized liquid-water permeability, infinitely thin CL and isothermal conditions [5–7,10–13]. For detailed reviews of steady-state modelling to the year 2004 the reader is referred to [14,15]. Notable exceptions to the steady-state trend are [16–21], none of which however include liquid-water transport or an energy balance, which are vital to an accurate description of flooding and membrane hydration. More comprehensive, fully two-phase models are found in [22,23]. The model in [23] is able to capture and predict the so-called "hysteresis" phenomenon observed in sweep cycling (of voltage or load), as well as its behaviour with respect to variations in the channel conditions.

Degradation phenomena have likewise received little attention in the modelling literature, particularly their incorporation into full MEA models. Modelling of membrane degradation is hampered by uncertainty in the reactions driving the structural changes [24]. On the other hand, due to the work of Springer et al. [25], Baschuk and Li [26–28] and Bhatia and Wang [29], good models for the kinetic mechanism of CO poisoning of the anode have been developed. This issue is of paramount importance as long as reformate gas is intended as the main source of H_2, whether on- or off-board a vehicle, until carbon-free pathways are developed, [30]. The concentration of CO in reformate can be as high as 100 ppm, which, because of its preferential adsorption, is extremely detrimental to performance. Of the methods to mitigate and reverse this process the two most widely studied are

1. Introduction of O_2 or air into the anode stream to enhance (provide an additional pathway for) CO oxidation on the Pt surfaces [31].
2. Alternative catalysts, for example platinum–ruthenium (Pt–Ru), that promote the production of oxygen-containing species such as hydroxyl (OH) and therefore provide an additional pathway for oxidation of CO from the Pt surfaces [32].

In the work of Springer et al. [25], the proposed CO poisoning mechanism was incorporated into a steady-state, single-phase model of the anode catalyst layer (ACL) and GDL. Baschuk and Li [27] placed the same mechanism inside a one-dimensional, steady-state, single-phase MEA framework, later extending their work to include the effects of O_2 bleeding using a more simplified MEA model [28]. A three-dimensional steady-state, single-phase phase model can be found in [33]. Bhatia and Wang [29] studied the transient problem by simplifying the kinetics proposed by Springer et al. and neglecting the transport phenomena, restricting their attention to the ACL. A similar model, which includes the diffusion of gas, can be found in [34]. A different approach can be found in [35], in which there is assumed to be a competition between linearly bonded and bridge-bonded adsorption, in contrast to the purely linear-bonded models in [25–29,33,34]. This model neglects the transport problem, is steady-state, employs temperature-independent rate constants and simplifies the CO adsorption kinetics. One of the aims of the latter work is to investigate the role of ruthenium (Ru), when alloyed with Pt, in resisting the CO poisoning. A more recent model of Pt–Ru, [36], takes the linear-bonded approach, concentrating solely on the kinetics of CO adsorption and oxidation in the ACL. A detailed discussion is postponed until Section 4.2.

The kinetics of CO poisoning, on either Pt or Pt–Ru, or of O_2 bleeding have yet to be incorporated in a two-phase MEA model, even under a steady-state, isothermal assumption. Flooding, membrane hydration, (averaged) microscopic properties such contact angle and pore size, and the evolution of the system in time will inevitably interact with and influence the kinetic problems—as we shall demonstrate by means of several examples. The aim of this paper is to incorporate these kinetic mechanisms in the transient, two-phase, non-isothermal model developed in [23] (in which its predictive capability is demonstrated) thereby extending CO modelling for PEMFC in several key areas simultaneously. The following features are included.

1. The entire MEA with explicit models of the GDL, membrane and both CL.
2. A full description of the transport of charge, mass (including dissolved reactants and liquid-water) and thermal energy in the multi-phase system.
3. The full kinetic models of Springer et al. and Baschuk and Li for CO poisoning and O_2 bleeding [25,28], and an augmented version of the model of Enbäck and Lindbergh for CO kinetics on Pt–Ru [36].
4. The mass-diffusion limitation in the cathode catalyst layer (CCL) using an agglomerate model.
5. Microstructural characterization of each component (in an averaged sense) and arbitrary (operating) conditions in the channel.

The resulting model has significant potential as a framework for a PEMFC code that is able to predict performance *and* degradation phenomena in realistic settings.

2. Model assumptions and equations

The various features and assumptions that form the basis of the model are now listed and briefly discussed (we refer to [23] for full details).

1. *One-dimensional full MEA transient*. The domain includes the entire MEA from the interface between the gas channels and GDL to the membrane (see Fig. 1). Each component is modelled explicitly.
2. *Catalyst layers*. We assume that the carbon support forms spherical clusters, referred to as *agglomerates*. Surrounding each agglomerate is an electrolyte layer, possibly surrounded by a layer of liquid-water. The pores between agglomerates are referred to as primary pores, distinct from the smaller pores between the carbon particles.
3. *Reactant and gas transport*. Diffusion in the primary pores of the CL is assumed to conform to Fick's law. The O_2 and H_2 in the primary pores of the CL reach the Pt particles on the agglomerate surfaces by adsorbing at the water/electrolyte surface and diffusing across the surrounding layers. Devia-

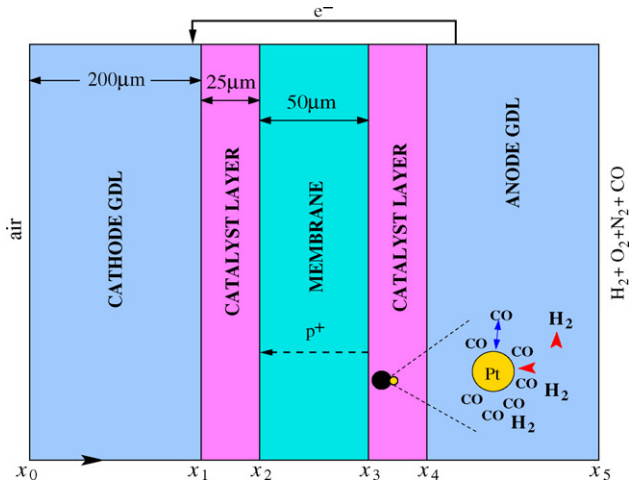

Fig. 1. Model geometry indicating the entry points of the reactants and contaminant, and the transport of protons and electrons.

tion from Henry's law (equilibrium) provides a driving force for interfacial mass transfer. As in [5,22,37] the steady-state Darcy's law is employed for the convective flow of gas.

4. *Proton and electron concentration*. The protons are assumed to be transported in the form of hydronium ions, H_3O^+. For both proton and electron transport we assume electroneutrality and a pseudo steady-state (see [38]).
5. *Water*. Water is considered to exist in three forms: as a dissolved species, as vapour and as liquid. We assume that the *net* water produced is in liquid form. Condensation and evaporation are modelled using the approach in [2,4,5], and references therein (dictated by the deviation of the local thermodynamic state from equilibrium). In a similar fashion, we introduce phase change between vapour and dissolved water and between liquid and dissolved water by considering the deviation from an equilibrium between the phases.
6. *Temperature*. A single temperature is assumed, amounting to an assumption of infinite rates of heat exchange between the phases.
7. *Kinetics*. The kinetics for CO poisoning are taken from [25], which have also formed the basis for the work in [26,27,29]. This model assumes linearly bonded CO and H_2 on Pt, with temperature, potential and coverage dependent rate constants. Kinetics for O_2 bleeding are taken from [28] and assume that the gas-phase oxidation of CO and H_2 is negligible. Those on Pt–Ru are an extension of the model in [36], which neglects the adsorption of CO on Ru and the H_2 kinetics entirely, and are based on the bifunctional mechanism proposed by Watanabe and Motoo [39].

2.1. Gas phase equations

Let s denote liquid-water (H_2O^{liq}) saturation, C_O, C_N, C_H, C_{CO}, C_{CO_2} and C_v, respectively the concentrations of O_2, N_2, H_2, CO, CO_2 and vapour (H_2O^{vap}) in the pore space, and $C_{i,e}$, $i \in \{O, H, CO, CO_2\}$, the concentrations of O_2, H_2, CO and CO_2 in the CL electrolyte and membrane. The subscript j refers to anode (a) and cathode (c). Mass balances yield

$$\frac{\partial}{\partial t}(\epsilon(1-s)C_i) - \frac{\partial}{\partial x}\left(D_{p,i}\frac{\partial C_i}{\partial x} - v_g C_i\right) = -S_{pi} \quad (1)$$

$$\frac{\partial}{\partial t}(\epsilon(1-s)C_N) - \frac{\partial}{\partial x}\left(D_N\frac{\partial C_N}{\partial x} - v_g C_N\right) = 0 \quad (2)$$

$$\frac{\partial}{\partial t}(\epsilon(1-s)C_v) - \frac{\partial}{\partial x}\left(D_v\frac{\partial C_v}{\partial x} - v_g C_v\right) = S_{ce} + \nu S_{ad} \quad (3)$$

where $D_{p,i}$, D_N and D_v, $i \in \{O, H, CO, CO_2\}$, are the diffusion coefficients of O_2, H_2, CO, CO_2, N_2 and vapour in the pore space (see the expressions in Table 7, in which T is temperature and P is gas pressure). The porosity ϵ takes the value $\epsilon = \epsilon_p$ in the CL and $\epsilon = \epsilon_g$ in the GDL.

The gas velocity is assumed to follow Darcy's law and the Kozeny–Carman law is used to approximate permeability

$$v_g = -\frac{\kappa}{\mu}(1-s)^3\frac{\partial P}{\partial x}, \quad \kappa = \frac{d^2}{K}\frac{\epsilon^3}{(1-\epsilon)^2} \quad (4)$$

where κ is the absolute permeability of the GDL or CL, μ is the dynamic viscosity of the gas, the factor $(1-s)^3$ is the relative permeability, d is a mean pore diameter and K is the Kozeny–Carman constant. The source terms are defined in Table 1. The quantity $\nu = 1800\,\mathrm{mol\,m^{-3}}$is the fixed-charge site concentration of the membrane, $h_{pe,i}$ are volumetric mass-transfer coefficients from gas to electrolyte (on the gas side) and H_i, $i \in \{O, H, CO, CO_2\}$, are dimensionless Henry constants. Each $h_{pe,i}$ is approximated based on a local Sherwood number of 2 (for flow past a spherical particle, [40]), $h_{pe,i} = (Sh D_{p,i} s_a)/(d) \geq O(10^5)$, where s_a is the specific surface area of the agglomerates. The condensation/evaporation coefficient h_{pc} is defined later.

2.2. Membrane and carbon phases

The electrolyte volume fraction, ϵ_e, has two components: one from the films that coat the agglomerates (ϵ_e^f) and the other from the electrolyte contained in the agglomerate interiors (ϵ_e^i), with $\epsilon_e = \epsilon_e^f + \epsilon_e^i$. To account for the volume change due to swelling (assumed to impact only the film thickness) we write $\epsilon_e^f = \epsilon_{e,0}^f + 0.0126\lambda$, where λ is the membrane water content (mol H_2O/mol

Table 1
Sources and sinks for the gas phase Eqs. (1)–(3)

	ACL	CCL	GDL	Meaning
S_{pi}	$h_{pe,i}(H_i C_i - C_{i,e})$	$h_{pe,i}(H_i C_i - C_{i,e})$	0	Reactant dissolution in electrolyte
S_{ce}	$-h_{pc}(X_v P - P_{sat})$	$-h_{pc}(X_v P - P_{sat})$	$-h_{pc}(X_v P - P_{sat})$	Condensation/evaporation
S_{ad}	$h_{dv}(C_d - C_d^*)$	$h_{dv}(C_d - C_d^*)$	0	Vapour/dissolved water mass transfer

Table 2
Sources and sinks for the dissolved reactants, potential and dissolved-water Eqs. (6)–(8)

	ACL	CCL	Meaning
$S_{r,O}$	$-aq_{O,ads}$	$\mathcal{R}_O(\eta_c, T, C^s_{O,e})/4$	O_2 consumption
$S_{r,H}$	$-aq_{H,ads}$	0	H_2 consumption
$S_{r,CO}$	$-aq_{CO,ads}$	0	CO consumption
S_{r,CO_2}	$aq_{CO,ox} + aq_{C-O,ox}$	0	CO_2 production
S_{ϕ_e}	$aF(q_{H,ox} + 2q_{CO,ox})$	$FS_{r,O}$	Proton source/sink
S_{ϕ_s}	$-S_{\phi_e}$	$-S_{\phi_e}$	Electron source/sink
S_{dl}	$h_{dl}(C_d - C^*_{d,l})$	$h_{dl}(C_d - C^*_{d,l})$	Liquid/dissolved water mass transfer
S_w	$-aq_{CO,ox} + aq_{H-O,ox}$	$-2S_{r,O}$	Water production (liquid phase)

The last term represents liquid-water production in Eq. (11).

SO_3^-) and $\epsilon^f_{e,0}$ represents the volume fraction of film without any swelling. The latter quantity is related to the film thickness without swelling, $\delta_{e,0}$, as shown in Table 6 (see [23] for full details). The Pt inside the agglomerates is assumed to be inactive and the combined volume fraction of the carbon, Pt and small pores, ϵ_a, is assumed constant. The volume fraction of primary pores is thus $\epsilon_p = 1 - \epsilon_a - \epsilon_e$. Membrane water content satisfies

$$\lambda = \frac{C_d}{1 - 0.0126 C_d} \quad \text{where}$$

$$C_d = \frac{\text{dissolved water concentration(mol m}^{-3})}{\nu} \tag{5}$$

Equations for reactant concentration in the electrolyte and membrane are given by

$$\frac{\partial}{\partial t}(\epsilon C_{i,e}) - \frac{\partial}{\partial x}\left(\epsilon^{3/2} D_{i,e} \frac{\partial C_{i,e}}{\partial x}\right) = S_{r,i} + S_{pi} \tag{6}$$

where $\epsilon = \epsilon_e$ in the CL, $\epsilon = 1$ in the membrane and $D_{i,e}$, $i \in \{O, H, CO, CO_2\}$, are the diffusion coefficients (see Table 7) used with Bruggeman corrections. The source terms are defined in Table 2; the surface reaction rates q and the volumetric reaction rate $\mathcal{R}_O$ will be defined in Section 2.6. The quantity a is the volumetric specific surface area of catalyst.

Equations for potential in the electrolyte/membrane and carbon, ϕ_e and ϕ_s, respectively, are derived from conservation of charge (assuming electro-neutrality and steady-state)

$$-\frac{\partial}{\partial x}\left(\epsilon^{3/2}\sigma_e \frac{\partial \phi_e}{\partial x}\right) - S_{\phi_e} = -\frac{\partial}{\partial x}\left(\epsilon^{3/2}\sigma_s \frac{\partial \phi_s}{\partial x}\right) + S_{\phi_s} = 0 \tag{7}$$

where σ_e and σ_s are the protonic and electronic conductivity respectively (used with Bruggeman corrections) and F is Faraday's constant. $\epsilon = \epsilon_e$ in the CL and $\epsilon = 1$ in the membrane for ϕ_e, while $\epsilon = 1 - \epsilon_g$ in the GDL and $\epsilon = \epsilon_s$ in the CL for ϕ_s. The source terms are defined in Table 2 and the conductivities in Table 7.

The mass balance for water dissolved in the electrolyte is written as follows

$$\frac{\partial}{\partial t}(\epsilon C_d) - \frac{\partial}{\partial x}\left(\epsilon^{3/2} D_d \frac{\partial C_d}{\partial x} + \frac{5\lambda}{44F\nu}\epsilon^{3/2}\sigma_e \frac{\partial \phi_e}{\partial x}\right) = -S_{ad} - S_{dl} \tag{8}$$

in which $\epsilon = 1$ for the membrane and $\epsilon = \epsilon_e$ for the CL, and D_d is the diffusion coefficient for dissolved water, given in Table 7(note the Bruggeman correction). The source terms S_{ad} and S_{dl} are defined in Tables 1 and 2 respectively, and will also be discussed in Section 2.5.

2.3. Energy

The conservation of thermal energy is expressed as follows:

$$\frac{\partial}{\partial t}(\rho C_p T) + \frac{\partial}{\partial x}\left(\epsilon s \rho_l C_l v_l T + \epsilon(1-s)\rho_g C_g v_g T - k\frac{\partial T}{\partial x}\right) = \sum_k S_k \tag{9}$$

where ρ_l, ρ_g and ρ_s (C_l, C_g and C_s) are respectively the densities (specific heat capacities) of liquid, gas and solid, and k (ρC_p) is the volume averaged thermal conductivity (heat capacity)

$$k = k_p(1-s)\epsilon + k_l s\epsilon + k_s(1-\epsilon),$$
$$\rho C_p = \epsilon s \rho_l C_l + \epsilon(1-s)\rho_g C_g + \rho_s C_s(1-\epsilon) \tag{10}$$

where k_p, k_s and k_l are the thermal conductivities of the pore space, solid (averaged) and liquid-water respectively. In the GDL $\epsilon = \epsilon_g$ and in the catalyst layers $\epsilon = \epsilon_p$. In the membrane the only form of heat transport is conduction.

Table 3
Sources and sinks for the energy Eq. (9)

	Membrane	ACL	CCL	GDL	Meaning
S_{act}	0	$aF\eta_a q_{H,ox}$	$F\eta_c \mathcal{R}_O(\eta_c, T, C^s_{O,e})$	0	Activation losses
S_{rev}	0	$-\Delta_a T a q_{H,ox}$	$\Delta_c T \mathcal{R}_O(\eta_c, T, C^s_{O,e})$	0	Heat of reaction
S_{ohm}	$\sigma_e\left(\frac{\partial \phi_e}{\partial x}\right)^2$	$\sum_j \epsilon_j^{3/2}\sigma_j\left(\frac{\partial \phi_j}{\partial x}\right)^2$	$\sum_j \epsilon_j^{3/2}\sigma_j\left(\frac{\partial \phi_j}{\partial x}\right)^2$	$(1-\epsilon_g)^{3/2}\sigma_s\left(\frac{\partial \phi_s}{\partial x}\right)^2$	Ohmic losses
S_{pc}	0	$-h_{gl}S_{ce}$	$-h_{gl}S_{ce}$	$-h_{gl}S_{ce}$	Heat of evaporation

The quantity v_l is the liquid-water interstitial velocity and the source terms S_k are defined in Table 3. In these expressions $-\Delta_j$ is the entropy associated with ORR ($j = c$) and HOR ($j = a$) and h_{gl} is the liquid-gas enthalpy change for water.

2.4. Liquid phase

The mass balance of liquid-water is used with Darcy's law for the convective flux

$$\frac{\epsilon\rho_l}{W_l}\frac{\partial s}{\partial t} + \frac{\partial}{\partial x}\left(\frac{\epsilon\rho_l}{W_l}v_l\right) = -S_{ce} + \nu S_{dl} + S_w, \qquad v_l = -\frac{\kappa s^3}{\mu_l}\frac{\partial p}{\partial x} \tag{11}$$

where the source terms are defined in Tables 1 and 2, $\epsilon = \epsilon_g$ in the GDL and $\epsilon = \epsilon_p$ in the CL. W_l, v_l, μ_l and p are the molar mass, velocity, viscosity and pressure of liquid-water (with a relatively permeability of s^3 and absolute permeability κ). Since $p = P - p_c$, where p_c is capillary pressure, combining the equations above yields

$$\frac{\epsilon\rho_l}{W_l}\frac{\partial s}{\partial t} + \frac{\epsilon\kappa\rho_l}{\mu_l W_l}\frac{\partial}{\partial x}\left(s^3\left(\frac{\mathrm{d}p_c}{\mathrm{d}s}\frac{\partial s}{\partial x} - \frac{\partial P}{\partial x}\right)\right) = -S_{ce} + \nu S_{dl} + S_w \tag{12}$$

For a discussion on the form of the permeability and capillary pressure the reader is referred to [4,41]. In this paper we adopt the widely used Leverette-function found in, for example, [9]. In the GDL and CL the capillary pressure is defined as (respectively)

$$p_c = \sigma' \cos\theta_c^g \sqrt{\frac{\epsilon_g}{\kappa_g}}\mathcal{J}(1-s), \qquad p_c = \sigma' \cos\theta_c^c \sqrt{\frac{\epsilon_p}{\kappa_c}}\mathcal{J}(s) \tag{13}$$

where $\mathcal{J}(\xi) = 1.417\xi - 2.12\xi^2 + 1.262\xi^3$ is the Leverette function, σ' is surface tension, and θ_c^c and κ_c (θ_c^g and κ_g) are the contact angle and absolute permeability of the CL (GDL), respectively.

2.5. Water balance: phase change

Condensation/evaporation is driven by the deviation from equilibrium, $X_v P - P_{sat}$, where P_{sat} is the saturation pressure of water and the first term, in which X_v is the vapour mole fraction, is the partial pressure of the vapour

$$h_{pc} = k_c\frac{\epsilon_p(1-s)X_v}{RT} \quad \text{if} \quad X_v P > P_{sat} \quad \text{and}$$
$$h_{pc} = k_e\frac{\epsilon_p s\rho_l}{W_l} \quad \text{if} \quad X_v P < P_{sat} \tag{14}$$

in which k_c and k_e are the condensation and evaporation rate constants, whose values are taken from [2] (see Table 7).

In a similar fashion, the vapour-dissolved phase-change term in Eqs. (3) and (8) is driven by the deviation from equilibrium between the vapour and dissolved water, $C_d - C_d^*$, where C_d^* is the dissolved concentration at equilibrium (from [42])

$$\lambda^* = 0.3 + 10.8a_w - 16a_w^2 + 14.1a_w^3,$$
$$C_d^*(1 + 0.0126\lambda^*) = \lambda^* \tag{15}$$

$a_w = X_v P/P_{sat}$ is the water vapour activity. The mass-transfer coefficient h_{dv} is approximated from the results in [43]

$$h_{dv} = \kappa_a(1-s)\lambda \quad \text{if} \quad C_d - C_d^* < 0 \quad \text{and}$$
$$h_{dv} = \kappa_d(1-s)\lambda \quad \text{if} \quad C_d - C_d^* > 0 \tag{16}$$

where κ_d and κ_e are given in Table 7.

The equilibrium membrane water content depends on the environment, with either relationship (15) for contact with vapour or $\lambda = \lambda_l^* = 16.8$ (or $C_d = C_{d,l}^* = \lambda_l^*/(1 + 0.0126\lambda_l^*)$) for contact with liquid. The discontinuity between the vapour-saturated and liquid values is known as Schroeder's paradox. The mass-transfer term S_{dl} in Eqs. (8) and (11), and Table 2, is decomposed into terms for absorption and desorption of liquid-water to and from the electrolyte in the CL. When the liquid-equilibrated water content value $C_{d,l}^*$ is reached or exceeded, it is assumed that desorption of water from the electrolyte takes place (as liquid), the magnitude of which is driven by $C_d - C_{d,l}^*$. Adsorption is assumed to take place for $C_d < C_{d,l}^*$ provided $s > s_*$, where s_* is the immobile saturation. The term h_{dl} in Table 2 therefore takes the form

$$h_{dl} = k_{des}H(C_d - C_{d,l}^*) + k_{ads}H(s - s_*)H(-C_d + C_{d,l}^*) \tag{17}$$

where $H(\cdot)$ is the Heaviside function and k_{des} and k_{ads} are the coefficients of desorption and absorption, which, for simplicity, are assumed to be constant. Their values are chosen large enough that C_d does not overshoot $C_{d,l}^*$ significantly; see Table 7.

2.6. Reaction kinetics

In this section we define the reaction rates appearing in Table 2. The kinetics at the cathode are approximated as follows:

oxygen reduction reaction (ORR):

$$O_2 + 4H^+ + 4\,e^- \rightarrow 2H_2O \tag{18}$$

for which we use the Butler–Volmer law (in mol m^{-3} s^{-1})

$$\mathcal{R}_O(\eta_c, T, C_{O,e}^s) = \frac{a i_{ref,O}}{F C_{ref,O}}\epsilon_e C_{O,e}^s\,(e^{\alpha_a F\eta_c/RT} - e^{-\alpha_c F\eta_c/RT}) \tag{19}$$

with exchange current density $i_{ref,O}$, anodic and cathodic transfer coefficients α_a and α_c, reference reactant molar concentration $C_{ref,O}$, volumetric specific surface area of catalyst (per unit volume of catalyst layer) a and overpotential η_c. The expression $a = a_{pt}m_{pt}/L$ relates a to the mass specific Pt surface area (Pt surface area per unit mass of Pt), a_{pt}, the Pt loading, m_{pt}, and the CL thickness, L. The overpotentials in the cathode and anode, η_c and η_a respectively, are defined as

$$\eta_c = \phi_s - \phi_e - E_0, \qquad \eta_a = \phi_s - \phi_e \tag{20}$$

where E_0 is the open circuit potential, taken to be constant. We use an agglomerate model for the cathode in which $C_{O,e}^s$ is the oxygen concentration at the agglomerate surfaces. It is related to the bulk value, $C_{O,e}$, by balancing the rate of reaction with the rate of diffusion of reactant through an electrolyte/water film to the surfaces of the agglomerates. The final form of the reaction

rate is then

$$\mathcal{R}_{\mathrm{O}} = 4\gamma a' C_{\mathrm{O,e}} \frac{\mathrm{e}^{\alpha_a F\eta_c/RT} - \mathrm{e}^{-\alpha_c F\eta_c/RT}}{\gamma + a'\,(\mathrm{e}^{\alpha_a F\eta_c/RT} - \mathrm{e}^{-\alpha_c F\eta_c/RT})},$$

$$a' = \frac{a i_{\mathrm{ref,O}} \epsilon_{\mathrm{e}}}{4FC_{\mathrm{ref,O}}} \tag{21}$$

where γ is a measure of the diffusion rate through the films. It is approximated as follows:

$$\gamma = \frac{\gamma_{\mathrm{l}}\gamma_{\mathrm{e}}}{\gamma_{\mathrm{l}} + \gamma_{\mathrm{e}}}, \quad \text{where} \quad \gamma_{\mathrm{l}} = \frac{A' D_{\mathrm{l}}}{\delta_{\mathrm{l}}}, \qquad \gamma_{\mathrm{e}} = \frac{A D_{e,O}}{\delta_{\mathrm{e}}},$$

$$A' = 4\pi(R_{\mathrm{a}} + \delta_{\mathrm{e}})^2 N \tag{22}$$

in which δ_{e} (δ_{l}) is the electrolyte (water) film thickness, N is the number of agglomerates per unit volume, $A = 4\pi R_{\mathrm{a}}^2 N$ is the specific surface area of agglomerates (we assume that all of the surface area is covered), with agglomerate radius R_{a}, and D_{l} is the diffusion coefficient of O_2 through liquid-water. The film thicknesses, δ_{e} and δ_{l}, are defined in Table 6(taking into account electrolyte swelling). The reader is referred to [23] for a derivation.

It is commonly accepted that electrochemical CO oxidation in acidic solutions involves surface reaction between adsorbed CO and an oxygen-containing species [44]. On the anode we use the model proposed by Springer et al. in [25], based on the mechanism

$\mathrm{H_2}$ adsorption: $\mathrm{H_2 + 2M \rightleftharpoons 2(H\text{–}M)}$,

$\mathrm{H_2}$ electro-oxidation: $\mathrm{2(H\text{–}M) \rightleftharpoons 2H^+ + 2e^- + 2M}$,

CO adsorption: $\mathrm{CO + M \rightleftharpoons CO\text{–}M}$,

CO electro-oxidation:

$$\mathrm{CO\text{–}M + H_2O \rightleftharpoons M + CO_2 + 2H^+ + 2e^-} \tag{23}$$

where M represents a free Pt site. When O_2 is present in the anode, we assume that the gas-phase oxidation of CO and H_2 is negligible in comparison to oxidation by heterogeneous catalysis. Thus, the additional reactions are assumed to follow (see Baschuk and Li [28])

$\mathrm{O_2}$ adsorption: $\mathrm{O_2 + 2M \rightleftharpoons 2(O\text{–}M)}$,

CO heterogeneous oxidation: $\mathrm{CO\text{–}M + O\text{–}M \rightarrow CO_2 + 2M}$,

$\mathrm{H_2}$ heterogeneous oxidation: $\mathrm{O\text{–}M + 2(H\text{–}M) \rightarrow H_2O + 2M}$

(24)

which provides an additional path for CO oxidation, removing it from the Pt surfaces at a faster rate. Equations for the evolution of the site coverages θ_i, $i \in \{\mathrm{O, H, CO, M}\}$, are as follows (using notation similar to that in [28])

$$\rho\frac{\mathrm{d}\theta_{\mathrm{H}}}{\mathrm{d}t} = \underbrace{2k_{\mathrm{ads}}^{\mathrm{H}} C_{\mathrm{H,e}}\theta_{\mathrm{M}}^2 - b_{\mathrm{ads}}^{\mathrm{H}} k_{\mathrm{ads}}^{\mathrm{H}} \theta_{\mathrm{H}}^2}_{q_{\mathrm{H,ads}}} - \underbrace{2k_{\mathrm{ox}}^{\mathrm{H}}\theta_{\mathrm{H}}(\mathrm{e}^{\alpha_a F\eta_c/RT} - \mathrm{e}^{-\alpha_c F\eta_c/RT})}_{q_{\mathrm{H,ox}}} - \underbrace{2k_{\mathrm{ox}}^{\mathrm{H-O}}\theta_{\mathrm{O}}\theta_{\mathrm{H}}^2}_{q_{\mathrm{H-O,ox}}} \tag{25}$$

$$\rho\frac{\mathrm{d}\theta_{\mathrm{CO}}}{\mathrm{d}t} = \underbrace{k_{\mathrm{ads}}^{\mathrm{CO}} C_{\mathrm{CO},e}\theta_{\mathrm{M}}\,\mathrm{e}^{-\beta r\theta_{\mathrm{CO}}/RT} - b_{\mathrm{ads}}^{\mathrm{CO}} k_{\mathrm{ads}}^{\mathrm{CO}}\theta_{\mathrm{CO}}\,\mathrm{e}^{(1-\beta)r\theta_{\mathrm{CO}}/RT}}_{q_{\mathrm{CO,ads}}} - \underbrace{2k_{\mathrm{ox}}^{\mathrm{CO}}\theta_{\mathrm{CO}}\sinh(F\eta_{\mathrm{a}}/2RT)}_{q_{\mathrm{CO,ox}}} - \underbrace{k_{\mathrm{ox}}^{\mathrm{C-O}}\theta_{\mathrm{O}}\theta_{\mathrm{CO}}}_{q_{\mathrm{CO-O,ox}}} \tag{26}$$

$$\rho\frac{\mathrm{d}\theta_{\mathrm{O}}}{\mathrm{d}t} = \underbrace{2k_{\mathrm{ads}}^{\mathrm{O}} C_{\mathrm{O,e}}\theta_{\mathrm{M}}^2 - b_{\mathrm{ads}}^{\mathrm{O}} k_{\mathrm{ads}}^{\mathrm{O}}\theta_{\mathrm{O}}^2}_{q_{\mathrm{O,ads}}} - k_{\mathrm{ox}}^{\mathrm{H-O}}\theta_{\mathrm{O}}\theta_{\mathrm{H}}^2 - k_{\mathrm{ox}}^{\mathrm{C-O}}\theta_{\mathrm{O}}\theta_{\mathrm{CO}} \tag{27}$$

$$\theta_{\mathrm{M}} = 1 - \theta_{\mathrm{H}} - \theta_{\mathrm{O}} - \theta_{\mathrm{CO}} \tag{28}$$

We are assuming: H_2 and O_2 (dissociative) adsorption and desorption based on Langmuir isotherms ($q_{\mathrm{H,ads}}$ and $q_{\mathrm{O,ads}}$); Butler–Volmer kinetics for electro-oxidation of H_2 and CO ($q_{\mathrm{H,ox}}$ and $q_{\mathrm{CO,ox}}$); CO adsorption and desorption based on a Frumkin isotherm ($q_{\mathrm{CO,ads}}$); and Langmuir–Hinshelwood kinetics for the heterogeneous oxidation of CO and H_2 ($q_{\mathrm{H-O,ox}}$ and $q_{\mathrm{CO-O,ox}}$). The quantity ρ is the molar area density of catalyst sites.

The Frumkin kinetics [45] for CO adsorption and desorption were proposed by Springer et al. [25] (see references therein) based on analysis of the dependence of the critical current density on θ_{CO}. The same approach is adopted here, including the dependence of the forward step on θ_{CO}, with symmetry factor β and interaction parameter r. The Langmuir model assumes that coverage does not exceed a monolayer, that there is no interaction between adsorbed molecules and that the apparent standard free energy of adsorption is coverage-independent. The Frumkin model assumes that this energy varies linearly with θ_{CO} (each additional molecule adsorbs with less ease). The interaction parameter is the slope of this variation [46]. Note that this dependence was neglected by Bhatia and Wang [29], as well as the second-order nature of the intermediate hydrogen step proposed by Springer et al. Following Baschuk and Li [28], the rate constants are assumed to be of the Arrhenuis type

$$k_j^{\mathrm{i}} = k_{j,0}^{\mathrm{i}}\,\mathrm{e}^{-E_{j,k}^{\mathrm{i}}/RT}, \qquad b_j^{\mathrm{i}} = b_{j,0}^{\mathrm{i}}\,\mathrm{e}^{-E_{j,b}^{\mathrm{i}}/RT} \tag{29}$$

The pre-exponential factors and activation energies are listed in Table 4 and their values will be discussed in Section 3.1.

When Pt is replaced with Pt–Ru, these equations require modification. The kinetics in that case, including the adsorption of water and formation of hydroxyl radicals (OH), are presented and discussed in Section 4.2.

2.7. Initial-boundary conditions, numerical details and parameters

For the discussion on the boundary conditions we recall Fig. 1. At the interfaces between the membrane and CL, $x = x_2$ and $x = x_3$, the gas-phase and liquid-water fluxes are taken to be zero; that is, the gas species and liquid-water are assumed not to penetrate the membrane. Similarly, we assume that the fluxes of protons and dissolved species at the interfaces between the

Table 4
Pre-exponential factors and activation energies for the rate coefficients (29) in the system (25)–(28)

	Adsorption	Desorption	Electro-oxidation
H_2	$k^{H}_{ads,0} = 3\,m\,s^{-1}$	$b^{H}_{ads,0} = 4.18 \times 10^{11}\,mol\,m^{-3}$	$k^{H}_{ox,0} = 23.1\,mol\,m^{-2}\,s^{-1}$
	$E^{H}_{ads,k} = 10.4\,kJ\,mol^{-1}$	$E^{H}_{ads,b} = 87.9\,kJ\,mol^{-1}$	$E^{H}_{ox,k} = 16.7\,mol\,m^{-2}\,s^{-1}$
CO	$k^{CO}_{ads,0} = 3 \times 10^{4}\,m\,s^{-1}$	$b^{CO}_{ads,0} = 6.87 \times 10^{3}\,mol\,m^{-3}$	$k^{CO}_{ox,0} = 3.4 \times 10^{9}\,mol\,m^{-2}\,s^{-1}$
	$E^{CO}_{ads,k} = 47.3\,kJ\,mol^{-1}$	$E^{CO}_{ads,b} = 100\,kJ\,mol^{-1}$	$E^{CO}_{ox,k} = 127\,mol\,m^{-2}\,s^{-1}$
O_2	$k^{O}_{ads,0} = 6 \times 10^{15}\,m\,s^{-1}$	$b^{O}_{ads,0} = 1.36 \times 10^{36}\,mol\,m^{-3}$	
	$E^{O}_{ads,k} = 14.2\,kJ\,mol^{-1}$	$E^{O}_{ads,b} = 250\,kJ\,mol^{-1}$	
			Heterogeneous oxidation
H—O			$k^{H-O}_{ox,0} = 3.28 \times 10^{4}\,mol\,m^{-2}\,s^{-1}$
			$E^{H-O}_{ox,k} = 65.9\,kJ\,mol^{-1}$
C—O			$k^{C-O}_{ox,0} = 8.3 \times 10^{7}\,mol\,m^{-2}\,s^{-1}$
			$E^{C-O}_{ox,k} = 90\,kJ\,mol^{-1}$

CL and GDL, $x = x_1$ and $x = x_4$, are negligibly small

$$\frac{\partial C_{i,e}}{\partial x} = \frac{\partial \phi_e}{\partial x} = D_d \frac{\partial C_d}{\partial x} + \frac{5\lambda\sigma_e}{44Fv}\frac{\partial \phi_e}{\partial x} = 0\,(x = x_1, x_4),$$
$$\frac{\partial C_i}{\partial x} = \frac{\partial s}{\partial x} = 0\,(x = x_2, x_3) \tag{30}$$

At the interfaces between the channels and GDL, the gas concentrations, temperature, water activity and pressure are prescribed. The cell voltage, V_{cell}, is prescribed at the cathode channel/GDL interface, and at the anode channel/GDL interface we assume a zero concentration of electrons.

$$C_i(x_0) = \bar{C}_{i,c}, \quad C_i(x_5) = \bar{C}_{i,a} \;\; i \in \{H, O, CO, CO_2, N, v\},$$
$$\phi_s(x_0) = V_{cell}, \quad \phi_s(x_5) = 0, \quad T(x_0) = T_c, \quad T(x_5) = T_a,$$
$$P(x_0) = P_c, \quad P(x_5) = P_a, \quad a_w(x_0) = a_{w,c}, \quad a_w(x_5) = a_{w,a} \tag{31}$$

The values of $\bar{C}_{v,c}$ and $\bar{C}_{v,a}$ are calculated from the water activity. The saturation pressure in atm, a function of temperature, is given by the formula in [47]

$$\log_{10} P_{sat} = -2.1794 + 0.02953\Delta T - 9.1837 \times 10^{-5}\Delta T^2 + 1.4454 \times 10^{-7}\Delta T^3 \tag{32}$$

where $\Delta T = T - 273$. From these relationships we obtain $\bar{C}_{v,c} = a_{w,c} P_{sat,c}/RT_c$, where $P_{sat,c}$ is the cathode-channel saturation pressure. A similar calculation applies on the anode side.

The final boundary conditions are those for liquid-water at the interfaces between the gas channels and the GDL. We approximate them with the following steady-state flux conditions at $x = x_0$ and $x = x_5$ (see [23] for details)

$$\frac{\partial s}{\partial x} - \Omega_j s = 0, \quad j \in \{a, c\} \tag{33}$$

where $\Omega_j = 0$ corresponds to zero water removal from the anode channel, $j = a$, or cathode channel, $j = c$. Ω_j is likely to depend sensitively on the flow rate in the channel [48].

Initial conditions for pressure, temperature and vapour concentrations are consistent with the conditions in the channels. The water content of the membrane/electrolyte is assumed to be given by equilibrium with vapour in the channels. The saturation at the initial time is assumed zero.

Table 5
Channel conditions assumed in the calculations, unless otherwise specified

Symbol	Quantity	Size
T_c	Cathode channel temperature	70 °C
T_a	Anode channel temperature	70 °C
$a_{w,c}$	Cathode channel water activity	1
$a_{w,a}$	Anode channel water activity	1
$\bar{C}_{O,c}$	Oxygen concentration in cathode channel	$18.13\,mol\,m^{-3}$
$\bar{C}_{H,a}$	Hydrogen concentration in anode channel	$34.52\,mol\,m^{-3}$
P_c	Gas pressure in the cathode channel	300 kPa
P_a	Gas pressure in the anode channel	300 kPa
$\bar{C}_{v,c}$	Vapour concentration in cathode channel	$15.91\,mol\,m^{-3}$
$\bar{C}_{v,a}$	Vapour concentration in the anode channel	$15.91\,mol\,m^{-3}$
Ω_j	Liquid-water removal constants (anode and cathode)	$0.075\,m^{-1}$ (assumed)

Table 6
Unless otherwise specified these parameter values, relating to structural and electrochemical properties, were used in the calculations

Symbol	Quantity	Size	Ref.
Structural			
L	Catalyst layer thickness	25 μm	assumed
L_m	Membrane thickness	50 μm	Assumed
L_g	GDL thickness	200 μm	Assumed
ϵ_e^i	Electrolyte volume fraction in agglomerates	0.15	Assumed
ϵ_a	Volume fraction of agglomerates	0.4215	[55]
ϵ_s	Volume fraction of carbon in CL	0.2	Estimated
ϵ_g	Porosity of the GDL	0.74	[56]
R_a	Agglomerate radius	0.5 μm	[55]
$\delta_{e,0}$	Electrolyte film thickness w/o swelling	0.1 μm	[23]
$\epsilon_{e,0}^f$	Electrolyte volume fraction w/o swelling	$\frac{4\pi N}{3}[(R_a+\delta_{e,0})^3 - R_a^3]$	[23]
δ_e	Electrolyte film thickness (m)	$\sqrt[3]{R_a^3 + \frac{3\epsilon_e^f}{4\pi N}} - R_a$	[23]
δ_l	Water film thickness (m): $R_\delta = R_a + \delta_e$	$\sqrt[3]{R_\delta^3 + \frac{3s\epsilon_p}{4\pi N}} - R_\delta$	[23]
N	Agglomerate density	$5.8 \times 10^{17}\ m^{-3}$	Estimated
a_{pt}	Specific surface area of Pt	$1000\ cm^2\ (mg\ Pt)^{-1}$	[57]
m_{pt}	Pt loading	$0.4\ (mg\ Pt)\ cm^{-2}$	[3]
θ_c^c (θ_c^g)	Catalyst-layer (GDL) contact angle	90° (120°)	[58]
d_g	GDL pore size	10 μm	Assumed
d_c	Catalyst-layer pore size	2 μm	Assumed
Electrochemical			
$i_{ref,O}$	Cathode exchange current density	$10^{-2}\ A\ m^{-2}$	[22]
$C_{ref,O}$	Reference O_2 concentration	$0.05\ mol\ m^{-3}$	Assumed
α_c	Cathodic transfer coefficient	0.55	Measured
α_a	Anodic transfer coefficient	0.45	Measured
β	Symmetry factor	0.1	[28]
r	Interaction parameter	$39.77\ kJ\ mol^{-1}$	[28]
β_2	Symmetry factor (H_2O)	0.5	[36]
r_2	Interaction parameter (H_2O)	$1.34\ kJ\ mol^{-1}$	[36]
E_0	Open circuit potential	0.95 V	Assumed
ρ	Molar area density of Pt sites	$0.01042\ mol\ m^{-2}$	[29]
ρ_{Ru}	Molar area density of Ru sites	$\rho/2\ mol\ m^{-2}$	Variable
k_1	Forward rate constant (CO oxidation)	$10^{-7}\ mol\ m^{-2}\ s^{-1}$	Fitted
k_{-1}	Backward rate constant (CO oxidation)	$10^{-9}\ mol\ m^{-2}$	Fitted
k_2	Forward rate constant (H_2O adsorption)	$4 \times 10^{-7}\ mol\ m^{-2}\ s^{-1}$	[36]
k_{-2}	Backward rate constant (H_2O adsorption)	$9 \times 10^{-8}\ mol\ m^{-2}$	[36]
$-\Delta_c$	Entropy associated with ORR	$163.7\ J\ mol^{-1}K^{-1}$	[59]
$-\Delta_a$	Entropy associated with HOR[2]	$0\ J\ mol^{-1}K^{-1}$	[59]

The initial-boundary value problem was solved in COMSOL 3.2a, on a uniform grid (typically 128 points) using quartic Lagrange polynomials as trial and test functions. The switch functions were substituted with hyperbolic tangent functions to smooth the discontinuities, a standard procedure.

The default set of parameter values is given in Tables 5–7 . Parameter fitting of some of the electrochemical rate constants was found to be necessary, as in [25–29,33,34]. Several other parameters are estimated (as indicated in Tables 5–7), and the rest are found from the literature (with references provided).

3. Results and discussion

3.1. Validation and dependence on concentration

As a confirmation that the kinetics have been correctly captured we first compare our results to the experimental data collected by Bhatia and Wang [29], for temporal variations in the current density at a fixed cell voltage, under several CO concentrations. To reproduce those results we use pressures of 3 atm and temperatures of 80 ° C on both anode and cathode, with fully saturated conditions ($a_w = 1$ in both channels). Operation at 0.6 V for 2 h with zero CO concentration was simulated. On completion CO was introduced in the anode stream at different concentrations and calculations were continued to simulate 2 h of poisoning, for both 40%H_2/N_2/CO and H_2/CO. The results are demonstrated in Fig. 2, in which it can be seen that for 40%H_2/N_2/CO the current density drops substantially, by around 60% for CO concentrations of 10 ppm and by around 90% at 100 ppm. With H_2/CO the degradation is less severe at fixed concentrations of CO. This figure is to be compared with the experimental results in Fig. 6 of [29]; the trends are captured correctly, with respect to the concentration of both CO and H_2.

Fig. 3 shows the evolution of CO surface coverage, θ_{CO}, in the two cases of 10 and 100 ppm in 40%H_2/N_2/CO. Even at 10 ppm the level of CO is extremely high, indicating that CO coverage must be close to a monolayer before its effect on the the current density is strongly felt, the reason for this being the (relatively)

Table 7
Heat, charge and mass transfer/transport properties used in the calcu lations, unless otherwise specified

Symbol	Quantity	Size	Ref.
$D_{p,O}$	O_2 diffusion coefficient	$4.23 \times 10^{-9}(\epsilon(1-s)T)^{3/2}/P\ m^2\ s^{-1}$	[40]
$D_{p,H}$	H_2 diffusion coefficient	$1.43 \times 10^{-8}(\epsilon(1-s)T)^{3/2}/P\ m^2\ s^{-1}$	[40]
D_v	Vapour diffusion coefficient	$5.27 \times 10^{-9}(\epsilon(1-s)T)^{3/2}/P\ m^2\ s^{-1}$	[40]
$D_{p,CO}$	CO diffusion coefficient	$4.12 \times 10^{-9}(\epsilon(1-s)T)^{3/2}/P\ m^2\ s^{-1}$	[40]
D_{p,CO_2}	CO_2 diffusion coefficient	$3.6 \times 10^{-9}(\epsilon(1-s)T)^{3/2}/P\ m^2\ s^{-1}$	[40]
D_N	N_2 diffusion coefficient	$3.6 \times 10^{-9}(\epsilon(1-s)T)^{3/2}/P\ m^2\ s^{-1}$	[40]
D_d	Diffusion coefficient for H_2O^{dis}	$4.17 \times 10^{-8}\lambda(1+161\,e^{-\lambda})\,e^{-2436/T}\ m^2\ s^{-1}$	[60]
D_l	O_2 diffusivity in H_2O^{liq} (60 °C)	$4.88 \times 10^{-9}\ m^2\ s^{-1}$	[40]
$D_{e,O}$	O_2 diffusivity in Nafion	$3.1 \times 10^{-7}e^{-2768/T}\ m^2\ s^{-1}$	[61]
$D_{e,H}$ [a]	H_2 diffusivity in Nafion	$6.92 \times 10^{-9}\ m^2\ s^{-1}$	[62]
$D_{e,CO}$ [a]	CO diffusivity in Nafion	$4.38 \times 10^{-9}\ m^2\ s^{-1}$	[62]
D_{e,CO_2} [a]	CO_2 diffusivity in Nafion	$4.12 \times 10^{-9}\ m^2\ s^{-1}$	[62]
$h_{pe,i}$	Mass transfer rates	$10^5\ s^{-1}$	Estimated
H_O [b]	O_2 Henry's law constant	0.15	[16]
H_H [b]	H_2 Henry's law constant	0.63	[6]
H_{CO} [a]	CO Henry's law constant	0.32	
H_{CO_2} [a]	CO_2 Henry's law constant	1.94	
κ_j (κ_g)	Absolute permeability of CCL (GDL)	10^{-13} (8.7×10^{-12}) m^2	[56,63]
μ_l	H_2O^{liq} viscosity	10^{-3} Pa s	[4]
μ	Dynamic viscosity air	1.8×10^{-5} Pa s	Estimated
μ	Dynamic viscosity H_2	8.4×10^{-6} Pa s	Estimated
σ'	Surface tension	$0.07\ N\ m^{-1}$	[4]
k	Catalyst layer thermal conductivity	$0.67\ W\ m^{-1}K^{-1}$	[64]
k_m	Membrane thermal conductivity	$0.67\ W\ m^{-1}K^{-1}$	[64]
k_g	GDL thermal conductivity	$1.67\ W\ m^{-1}K^{-1}$	[64]
$\rho_l C_l$	H_2O^{liq} heat capacitance	$4.187 \times 10^6\ J\ m^{-3}K^{-1}$	Estimated
$\rho_g C_g$	Air heat capacitance	$10^3\ J\ m^{-3}K^{-1}$	Estimated
$\rho_m C_m$	Membrane heat capacitance	$2.18 \times 10^6\ J\ m^{-3}K^{-1}$	Estimated
$\rho_c C_c$	Carbon heat capacitance	$1.61 \times 10^6\ J\ m^{-3}K^{-1}$	Estimated
$-\Delta_c$	Entropy associated with ORR	$163.7\ J\ mol^{-1}K^{-1}$	Lamp
$-\Delta_a$	Entropy associated with HOR[3]	$0\ J\ mol^{-1}K^{-1}$	[59]
σ_s	Electronic conductivity	$500\ S\ m^{-1}$	[65]
σ_e	Protonic conductivity	$e^{1286(1/303-1/T)}(0.514\lambda - 0.326)\ S\ m^{-1}$	[47]
k_{des}	H_2O^{liq} Desorption coefficient	100	Assumed
k_{ads}	H_2O^{dis} adsorption coefficient	10	Assumed
κ_a	Absorption constant	$10^{-6}\ m\ s^{-1}$	[43]
κ_d	desorption constant	$3.3 \times 10^{-6}\ m\ s^{-1}$	[43]
k_e	Evaporation coefficient	$100\ s^{-1}\ atm^{-1}$	[2]
k_c	Condensation coefficient	$100\ s^{-1}$	[2]

[a] Approximated by value in/for liquid-water at 60 °C.
[b] For a detailed discussion see [66].

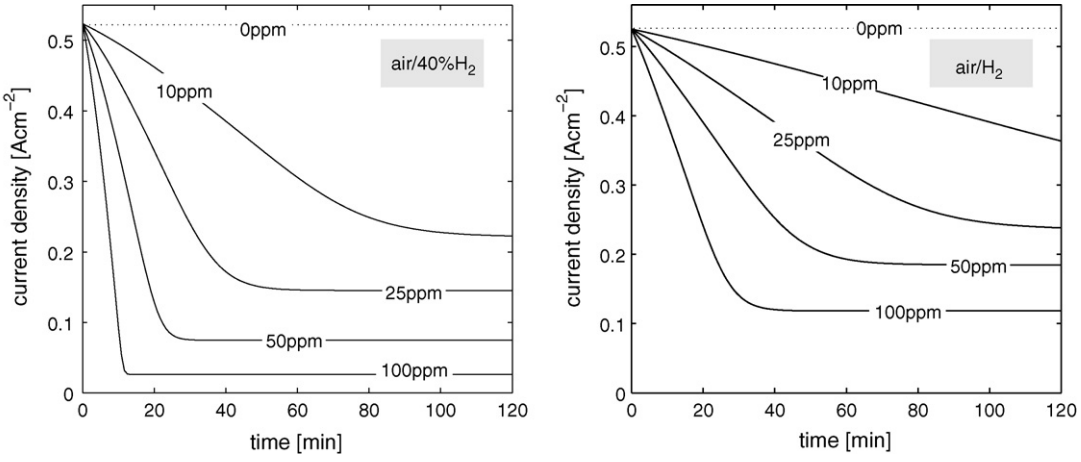

Fig. 2. Simulated evolution in the current density for several concentrations of CO in 40%H_2/N_2 and H_2. For a list of parameter values see Tables 5–7.

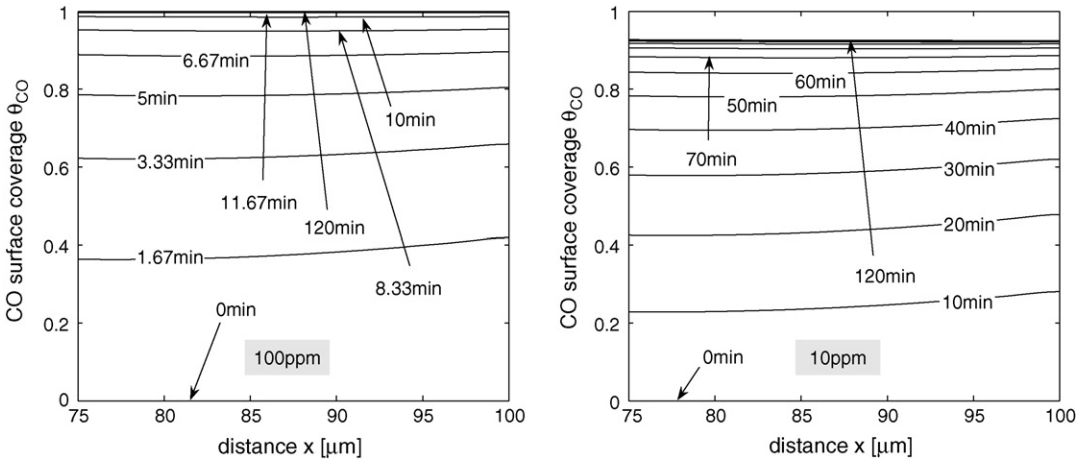

Fig. 3. Simulated profiles of CO surface coverage, θ_{CO}, for 100 ppm (left-hand figure) and 10 ppm (right-hand figure) of CO in 40%H_2/N_2, corresponding to the calculations in Fig. 2.

rapid rate of H_2 oxidation. The quantitative values are dependent on the parameters – those determining the rates of adsorption, desorption and oxidation – as was discussed in detail by Springer et al. [47]. Bhatia and Wang [29] adjusted the two parameters (assumed constant in their work) k^{H}_{ads} and b^{CO}_{ads} in order to match the experimental results. To achieve the correct qualitative trends a similar procedure was applied here with adjustments in $k^{H}_{ads,0}$ and $k^{CO}_{ox,0}$, the latter to a value close to that in [47] where it was approximately four orders of magnitude smaller than in the base case of [28]. In fact the corresponding term (CO heterogeneous oxidation) was neglected entirely by Bhatia and Wang [29] since it was deemed too small to contribute, at least at the cell voltages considered. The remaining values in Table 4 are taken from [28].

3.2. *Effects of cell voltage and sweep rate: potentiostatic sweep*

One of the effects not captured in the previous result (Fig. 2) is that of cell voltage on the extent of degradation. Of course, under steady-state conditions this effect is naturally contained in the polarization curves, which represent, generally speaking, the behaviour at time $t = \infty$ (i.e., sufficiently long for a 'steady-state' to be reached). In this section we present simulations of transient variations in the cell voltage (potentiostatic sweeps) for time scales smaller than those required for relaxation to steady-state. These experiments can yield results that are qualitatively similar to the steady-state curves but in general contain a richer structure [22,23,49].

The first result is shown on the left-hand side of Fig. 4, demonstrating the variation in performance with 40%H_2/N_2 and different CO concentrations. These curves are generated by a simulated voltage sweep from 1 to 0 V in 80 min. As with the steady-state polarization curves (see for example [25]) there are two characteristic turning points for large CO concentrations, one occurring at high cell voltage and marking the onset of poorer performance compared to 0 ppm, and one at a lower cell voltage, at which performance improves markedly. The explanation for these turning points is apparent from Fig. 5, which shows the simulated profiles of CO and H_2 surface coverage, θ_{CO} and θ_H, and simulated electro-oxidation rates, $aq_{CO,ox}$ and $aq_{H,ox}$, for 50 ppm.

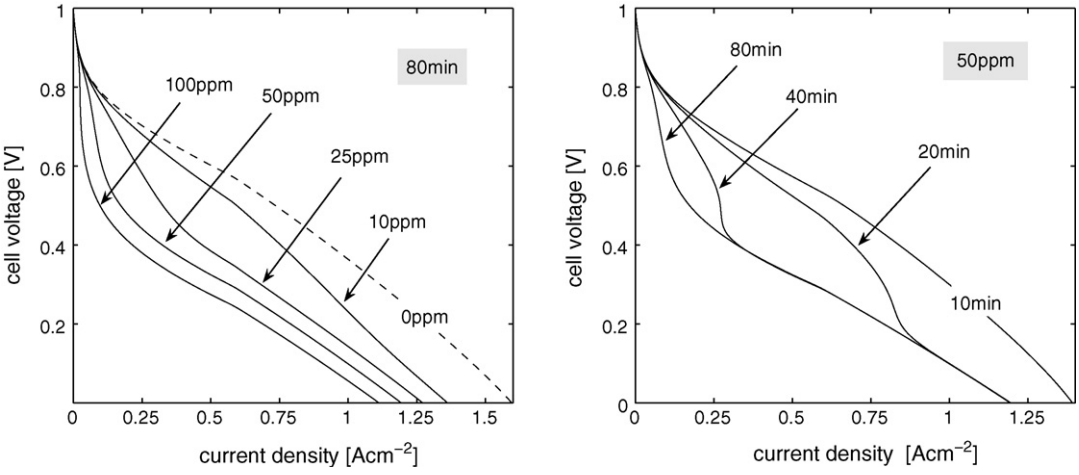

Fig. 4. The left-hand figure shows polarization curves from simulated voltage sweeps (1–0 V in 80 min) for a range of CO concentrations in 40%H_2/N_2. The right-hand figure demonstrates the effect of the sweep rate. The remaining parameter values are given in Tables 5–7.

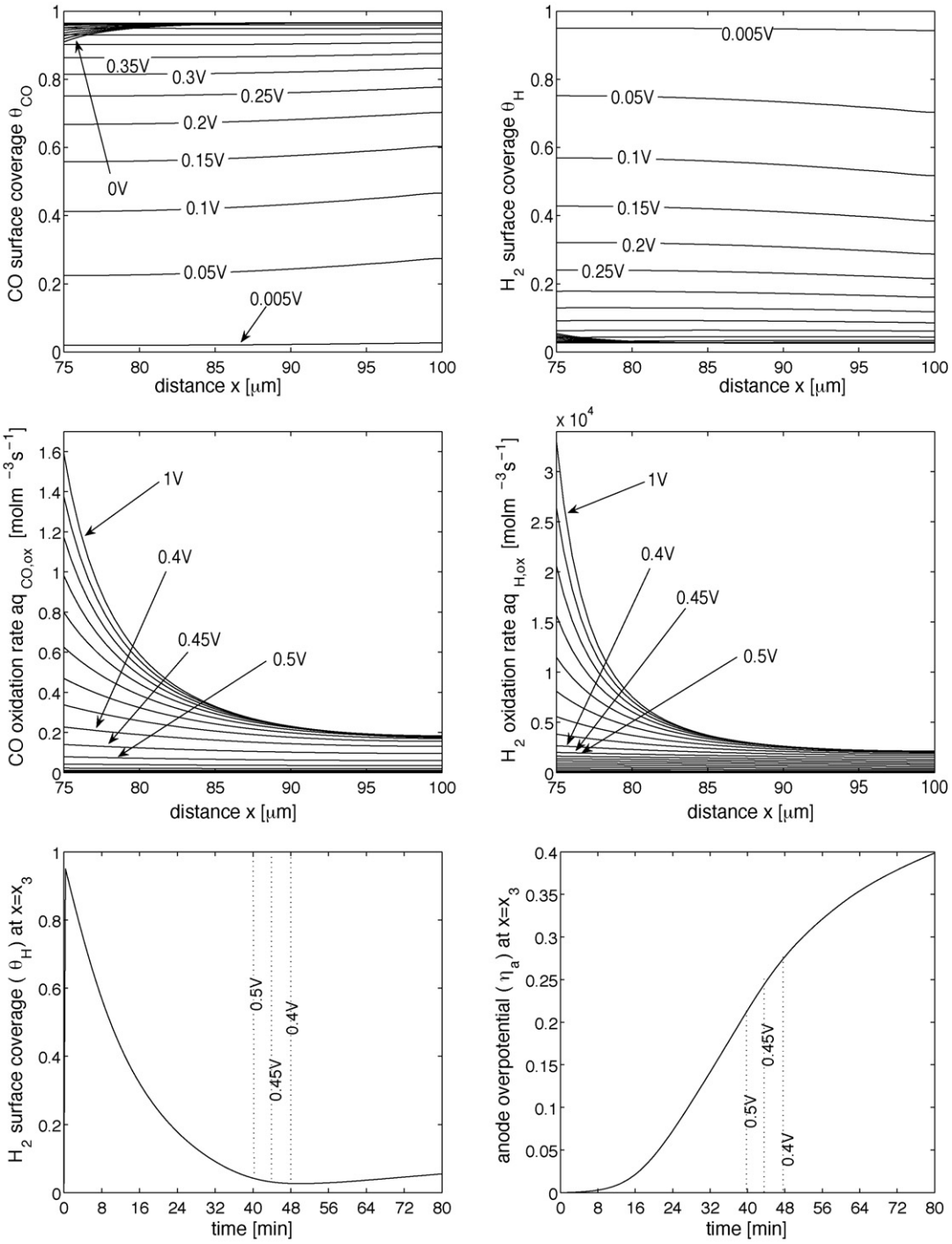

Fig. 5. The first two rows show simulated profiles of the surface coverage, θ_H and θ_{CO}, and the electro-oxidation rates, $aq_{H,ox}$ and $aq_{CO,ox}$. The bottom row shows the evolutions of anode overpotential, η_a, and H_2 surface coverage, θ_H, at the interface between the ACL and membrane, $x = x_3$. Note that these plots correspond to the calculation for 25 ppm CO in 40%H_2/N_2 on the left-hand side of Fig. 4: a potential sweep from 1 to 0 V in 80 min.

The first turning point is caused by the rapid coverage of sites, the extent of which increases with increasing CO concentration at fixed cell voltage (see Fig. 4). In the range of cell voltage between 1 V and the first turning point the rates of H_2 and CO oxidation are slow. At a cell voltage of approximately 0.45 V the rate of H_2 oxidation increases rapidly because of its exponential dependence on anode overpotential, the maximum in which evolves as shown in the bottom right of Fig. 5. This rapid increase leads to the second turning point in the curve in Fig. 4. Note that in [26] the authors postulate that increased CO electro-oxidation is the cause of the second turning point. This however seems an unlikely explanation given the magnitude of CO oxidation in comparison with that of H_2 (see Fig. 5); larger values of k_{ox}^{CO} will shift the location of the turning point to higher voltage values because of decreased CO coverage, but will not be the cause (see the steady-state results and discussion in [47]).

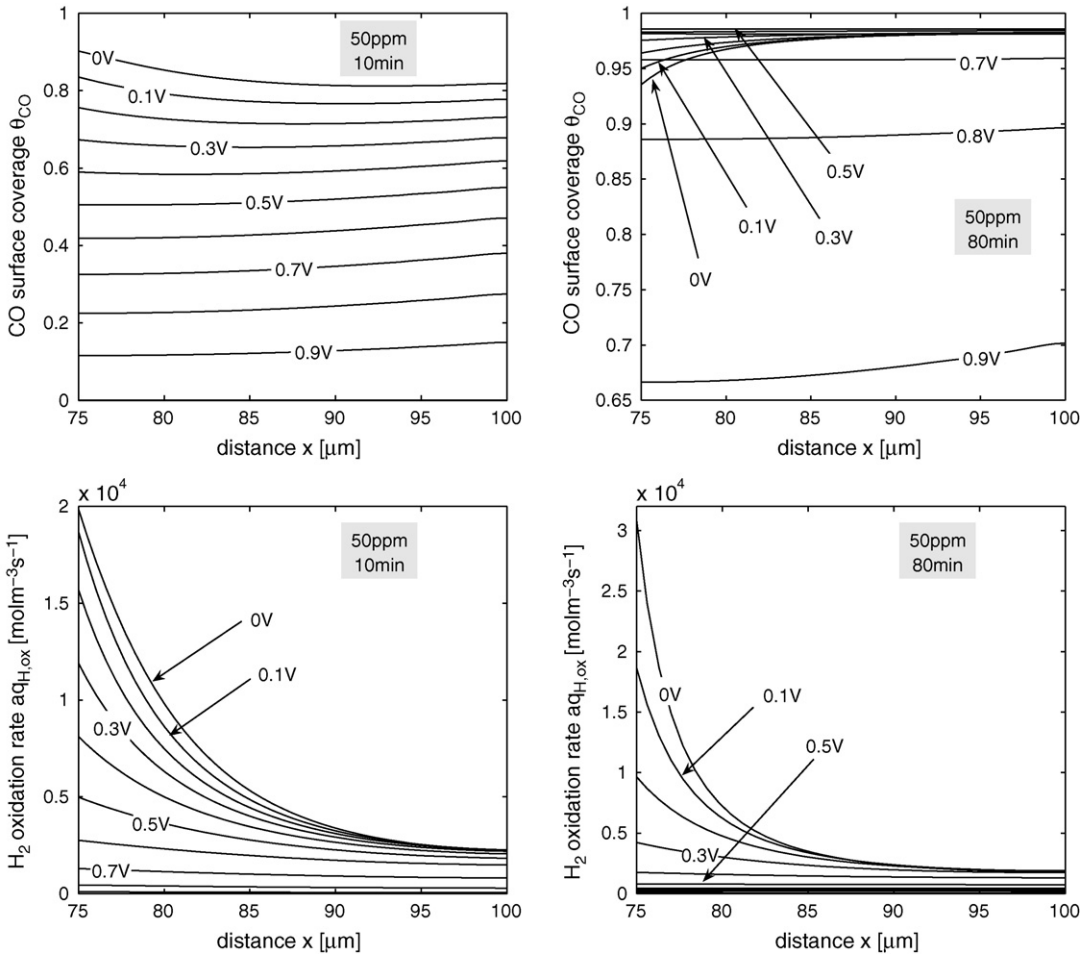

Fig. 6. Simulated profiles of CO surface coverage, θ_{CO}, and H_2 electro-oxidation rate, $aq_{H,ox}$, for 50 ppm in 40%H_2/N_2, corresponding to the calculations on the right-hand side of Fig. 4. The two cases shown here are for sweeps from 1 to 0 V in 10 min (left-hand column) and 80 min (right-hand column).

Unsurprisingly, the results contained in the left-hand side of Fig. 4 are dependant on the rate of decrease of the cell voltage (sweep rate). The right-hand side of Fig. 4 demonstrates the trend as the sweep time is decreased from 80 to 10 min. Clearly, the shorter the time the better the performance at fixed cell voltage; a manifestation of the decreasing time available to reach CO coverage levels that inhibit the H_2 oxidation substantially (see Fig. 6). The first turning point therefore occurs at a

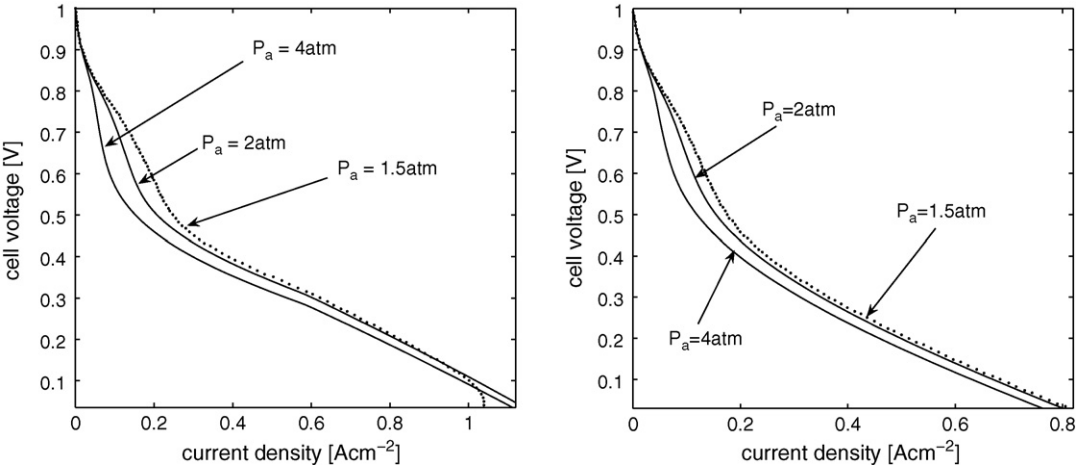

Fig. 7. Polarization curves generated from simulated potential sweeps (1–0 V in 80 min) with 50 ppm CO in 40%H_2/N_2, for a range of anode-channel pressure, P_a. Note than in the left-hand figure $a_{w,a} = a_{w,c} = 1$, whereas in the right-hand figure $a_{w,a} = a_{w,c} = 0.4$, in which case anode flooding is not apparent. The remaining parameter values are given in Tables 5–7.

lower cell voltage as the sweep rate is decreased. This has the natural consequence of shortening the distance in cell-voltage space between the the two turning points; by the time the CO coverage is significant the cell voltage is low enough to bring about the onset of the second turning point. At a low enough sweep rate the extent of CO coverage is too low to engender the first turning point, as illustrated in the 10 min sweep in Fig. 4.

3.3. Effects of anode channel pressure, temperature and humidity

The effect of anode channel pressure on the CO poisoning effect was investigated experimentally by Springer in [47]. It was found that increasing the anode pressure had a detrimental effect on performance, measured at steady-state, indicating that the kinetic order in free catalyst sites in Eq. (25) exceeds unity

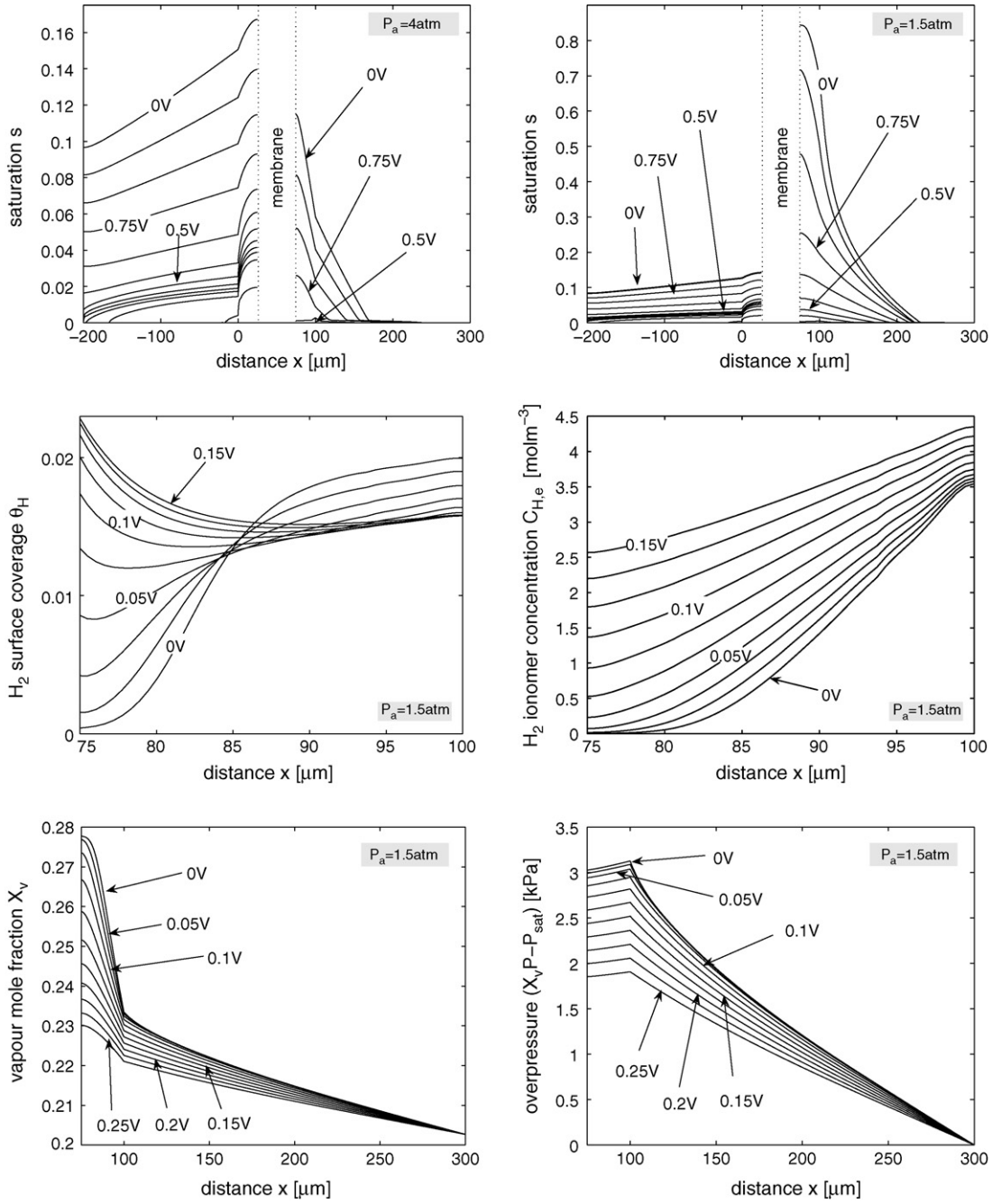

Fig. 8. The top row of figures shows simulated saturation profiles generated by a voltage sweep from 1 to 0 V in 80 min, with 50 ppm CO in 40%H_2/N_2, for two different anode-channel pressures (corresponding to Fig. 7). The middle row of figures shows the profiles of H_2 surface coverage and electrolyte concentration, θ_H and $C_{H,e}$ respectively, for the case $P_a = 1.5$ atm, in which the anode flooding severely restricts the access of H_2 to the Pt surfaces. The bottom row of figures demonstrates that the flooding is caused by saturation of the gas phase with vapour, with low levels of H_2 concentration and $a_{w,a} = 1$.

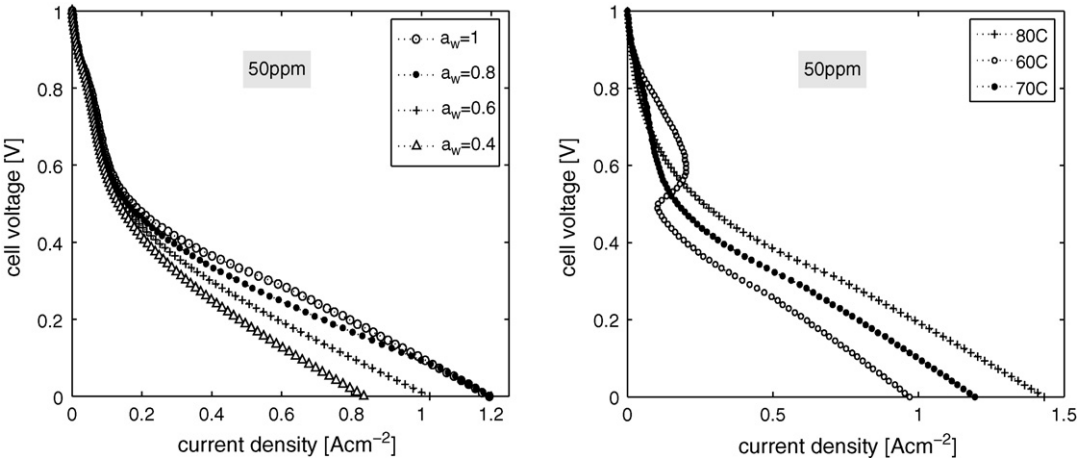

Fig. 9. Polarization curves generated from simulated potential sweeps (1–0 V in 80 min) with 50 ppm CO in 40%H_2/N_2, for a range of anode channel humidity (left hand figure with $T = 70^\circ$ C in both channels) and a range of channel temperature (right-hand figure with $a_{w,a} = a_{w,c} = 1$). The remaining parameter values are given in Tables 5–7.

(here assumed to be 2). For the transient case, while the same remains generally true for high anode pressures, the simulations presented next indicate that variations in anode pressure have a more convoluted effect, depending, in particular, on the the water activity in the channels.

Fig. 7 demonstrates that the steady-state experimental results in [47] (Fig. 8 of that paper) are qualitatively similar to potential sweeps from 1 to 0 V in 80 min, particularly for cell voltage away from the lower limit. Deviations from the steady-state trend arise at low values of anode channel pressure, for low cell voltage, where the performance deteriorates sharply. For an explanation we refer to Fig. 8, the top row of which shows the evolutions of the saturation profiles for the two extreme cases in Fig. 7: $P_a = 4$ and 1.5 atm. Clearly, the anode floods as the channel pressure is reduced, restricting the access of H_2 to the Pt particle surfaces and causing the sharp drop in performance observed in Fig. 7. The origin of the flooding is the low concentration of H_2, which leads to almost complete consumption in a region (in both the electrolyte and gas phases) close to the membrane/ACL interface (see the middle row of figures), locally forcing the gas pressure to decrease and molar fraction of vapour, X_v, to increase; the net result is an increasing overpressure $X_v P - P_{sat}$ (see the bottom row of Fig. 8) and therefore an increased rate of condensation, S_{ce}, defined in Table 1 and Eq. (14). Another important effect in this result will be the restricted back-diffusion of water through the membrane (from anode to cathode), compared to the case of $P_a = 4$ atm, because of the drop in the current density. This will lead to a greater retention of dissolved, and therefore liquid, water in the anode. Of course, this phenomenon is exacerbated by the fully humidified channel condition, $a_{w,a} = 1$. In fact, for $a_{w,a} = a_{w,c} = 0.4$, the flooding is not seen, as demonstrated on the right-hand side of Fig. 7. What is also noticeable is the better performance at $a_{w,a} = a_{w,c} = 1$, which can be attributed to the greater membrane water content (and therefore increased protonic conductivity) on the cathode side.

For high anode channel pressure the best performance is generally seen at $a_{w,a} = a_{w,c} = 1$, again because of the increased protonic conductivity, particularly on the cathode side. This is demonstrated in the polarization curves on the left-hand side of Fig. 9, for a range of channel humidity at the base-case anode pressure of 3 atm. Mass-transport limitations, arising from the cathode side, are noticeable at low cell voltage, manifested as an increasingly negative slope of the polarization curve: notice that the two cases $a_{w,a} = a_{w,c} = 1$ and $a_{w,a} = a_{w,c} = 0.8$ eventually cross. The results in Figs. 7 and 9 suggest that when CO is present in the anode stream the best performance is obtained for low anode pressure and high water activity in the cathode. When the cell is operated fully humidified in the anode channel there exists an optimal (low) anode pressure between 1.5 and 3 atm for which flooding in the anode can be avoided. Conversely, if the intention is to operate at an (low) anode pressure of 1.5 atm, there exist optimal channel water activities to avoid both flooding in the anode and severe mass-transport limitations in the cathode.

A further non-trivial observation is that mass transport limitations in the cathode, typically a major concern, seem to be less apparent when CO is present in the anode stream, even at high water activity. The lower current density with a CO-fed anode is the likely explanation; it leads to reduced water production and, simultaneously, reduced back diffusion of dissolved water from anode to cathode.

The effect of changes in the channel temperatures, at a fixed channel pressure, is shown on the right-hand side of Fig. 9. In general an increased temperature will enhance performance, primarily because of the increased membrane conductivity (see the form of σ_e in Table 7) and the resultant increased overpotential; the reaction rate (19) has an exponential dependence on overpotential, which outstrips the reduced concentration of reactants in the channels, on which the reaction rates have an algebraic dependence. This result on its own is not surprising but the transient aspect of the results does however reveal an important detail: as the temperature is lowered, in the upper part of the curve better performance is attained at fixed cell voltage. We refer to Fig. 10, which compares the evolutions of surface coverage, θ_H and θ_{CO}, and volumetric H_2 oxidation rate, $aq_{H,ox}$, at the two temperatures, evaluated at the interface between the membrane and ACL, $x = x_3$.

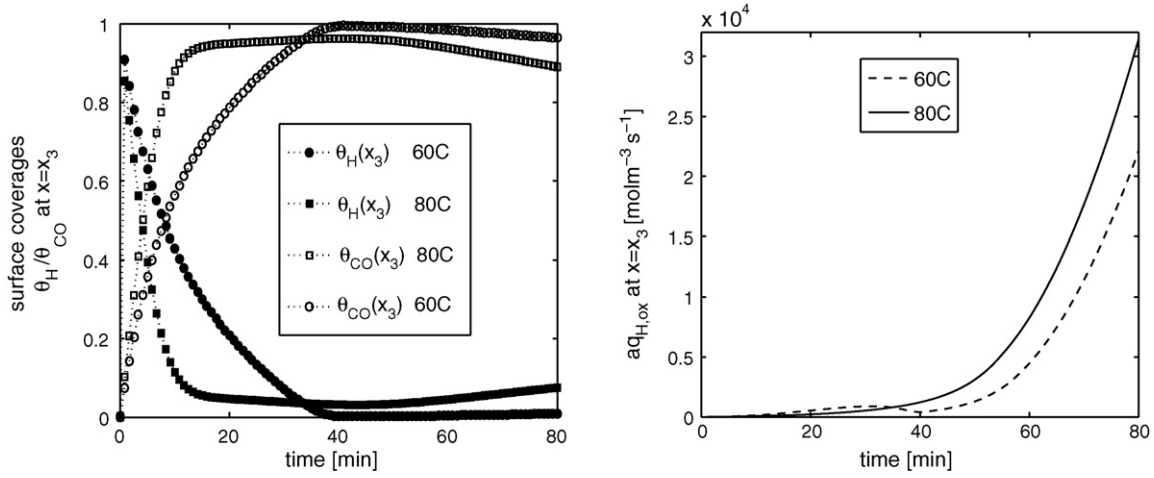

Fig. 10. The evolutions of surface coverages, θ_H and θ_{CO}, and H_2 oxidation rate, $aq_{H,ox}$, evaluated at the membrane/ACL interface, $x = x_3$, in the two cases $T_a = 60$ and 80 °C on the right-hand side of Fig. 9. These correspond to a simulated potential sweep from 1 to 0 V in 80 min, with 50 ppm CO in 40%H_2/N_2 and $a_{w,a} = a_{w,c} = 1$.

At the lower temperature CO (H_2) coverage is lower (greater) up to $t \approx 35$ min, with the opposite being true beyond this time. This clearly influences the relative shapes of the profiles in Fig. 10. However, this highly non-linear behaviour is not easy to predict. The lower temperature leads to reduced CO and H_2 adsorption rate constants through the Arrhenius activation energies (29) and the Frumkin term in (26). The rate constant for CO adsorption, k_{ads}^{CO}, experiences a more dramatic decrease than that for H_2 adsorption, k_{ads}^{H}, and therefore dominates, starting from the initial conditions of $\theta_{CO} = \theta_H = 0$ and zero desorption. The result is a lower CO coverage and (therefore) higher H_2 coverage. The desorption rate of CO increases as $\theta_{CO} \to 1$. However, in this limit the ratio of desorption to adsorption is proportional to $\exp((-100 + r\theta_{CO})/RT) \approx \exp(-60/RT)$, which is much smaller at the lower temperature. In other terms, the long-time value of CO coverage will be greater for the lower temperature, although in the early stages the CO coverage is lower. In summary, there is a sensitive balance between the decreasing rate of adsorption, decreasing rate of desorption and the decreased membrane hydration at the lower temperature. The evolution of reaction rate seen on the right-hand side of Fig. 10 (and therefore the curves seen in Fig. 9) is determined by this balance in a non-trivial way. Note that the final changes in the slopes of these curves at around $t = 50$ min coincide with the second turning points (H_2 oxidation) in the polarization curves.

4. Mitigation techniques

4.1. O_2 bleeding: CO pulse simulation and temperature effect

A known method for preventing the degradation seen in Fig. 2 is to inject air or neat O_2 into the anode fuel stream, the so-called O_2 bleeding method. The results of a series of transient experiments investigating O_2 bleeding can be found in [50,51], in which the cell voltage is measured for a constant load with time-varying compositions of H_2, CO and O_2. It was also found in these and other studies that a degraded cell has the capacity

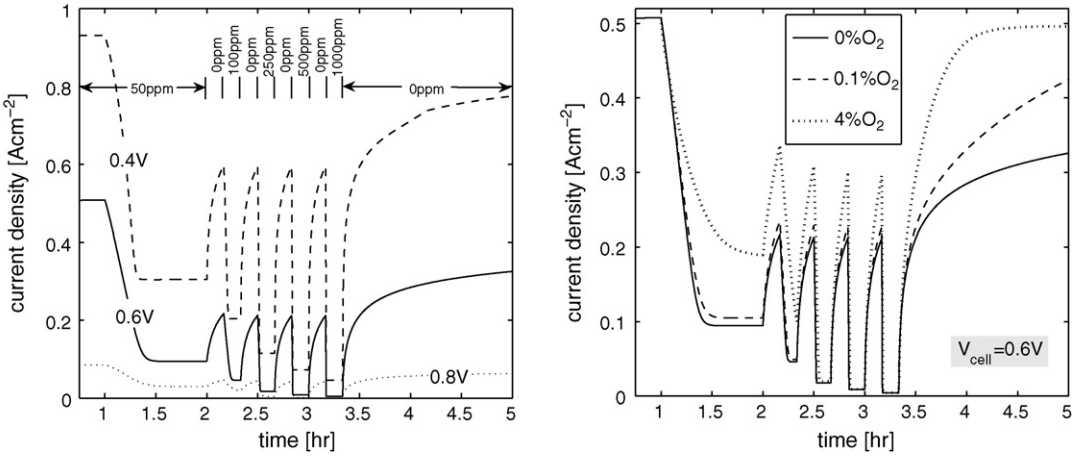

Fig. 11. The left-hand figure demonstrates the transient effect of CO pulsing and the ability of the system to recover for the indicated levels of CO at three cell voltage values. The right-hand figure demonstrates the effect of O_2 bleeding, at different concentrations in 40%H_2/N_2/CO, for a cell voltage of 0.6 V (remaining parameter values are given in Tables 5–7). The evolution of the surface coverages for 4% and 0.1% O_2 bleeding are demonstrated in Fig. 12.

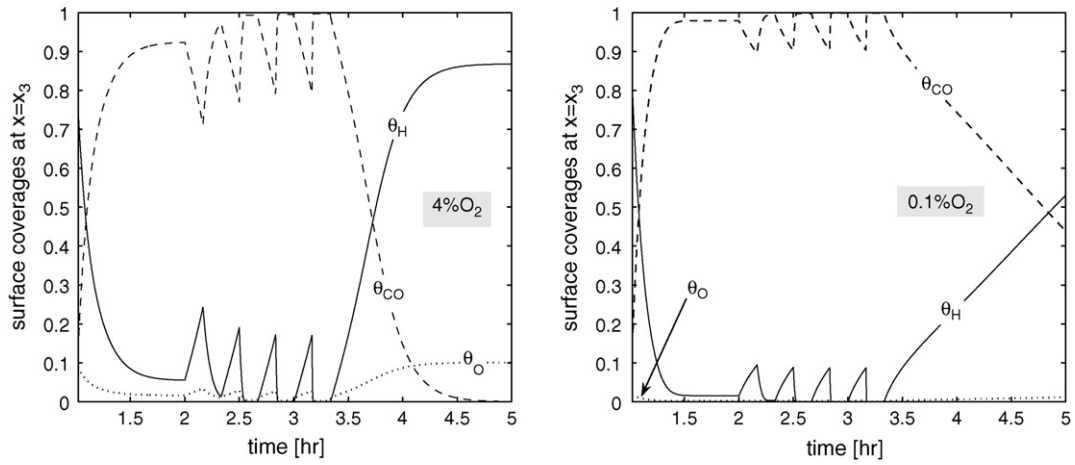

Fig. 12. Plots of O_2, CO and H_2 surface coverages evaluated at the interface between the ACL and membrane, $x = x_3$, corresponding to the examples on the right-hand side of Fig. 11 for 4% and 0.1% O_2 bleeding at 0.6 V.

to recover when fed with CO-free H_2, the extent of recovery depending on the initial input of CO and the poisoning and recovery times. We begin this section with simulations akin to the experiments in [50,51], instead calculating the current density as the cell voltage is varied with time-varying compositions of H_2, CO, O_2 and N_2. The main objective here is to demonstrate that qualitatively the outcome of such experiments can be predicted with the model.

We simulated 1 h of operation with 40%H_2/N_2/0 ppm CO in the anode and a fixed cell voltage (other parameters as in Tables 5–7), long enough to reach a steady current density. A concentration of 50 ppm CO was then introduced into the anode mixture for a further 1 h. Beyond $t = 2$ h the CO concentration was alternately set to zero for 10 min and to successively increased values for 10 min, eventually set to zero until $t = 5$ h. For $V_{cell} = 0.6$ V the calculations were then repeated with 40%H_2/0.1%O_2/N_2 and 40%H_2/4%O_2/N_2. The results are demonstrated in Fig. 11, the left-hand figure at three different cell voltages without bleeding and the right-hand figure at two different O_2 concentrations (in the anode channel) for $V_{cell} = 0.6$ V. From these plots we can make the following observations.

(1) The cell has a capacity to recover quite well by simply reversing to 40% H_2, even at a low cell voltage, as observed in the experiments in [29,50,51].
(2) On these relatively short time scales O_2 bleeding even at 4% does not significantly counter the poisoning effect when the CO concentration is high (particularly above 100 ppm), in agreement with the experimental results in [29,50,51]. Fig. 12 shows the evolutions of surface coverages evaluated at the membrane/ACL interface for the two anode oxygen concentrations; the CO coverages in the two cases are increasingly closer as the CO concentration is increased. Although not a proof, this latter result provides an indication that, as is known from experiment, there is an upper limit to the ameliorating effect of bleeding.

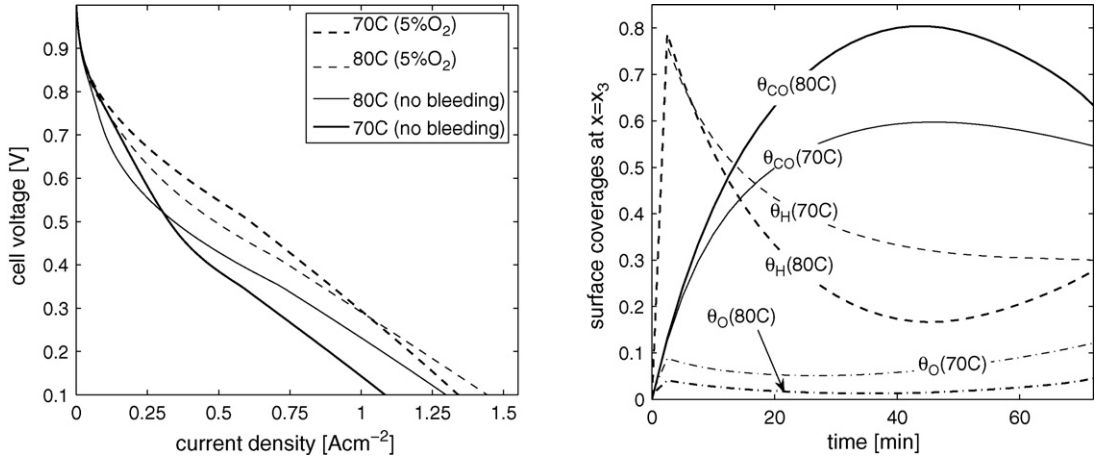

Fig. 13. The left hand figure shows polarization curves (from potential sweeps of 1–0 V in 80 min) with 25 ppm CO in 40%H_2/N_2/O_2, comparing bleeding with non-bleeding at two channel temperatures. The remaining parameter values are given in Tables 5–7. The right-hand figure shows the evolutions of surface coverages evaluated at the interface between the ACL and membrane, $x = x_3$, in both cases.

A more striking feature of the transient operation is seen when the channel temperatures are varied. The left-hand side of Fig. 13 compares bleeding with non-bleeding at two channel temperatures (same in both channels). These polarization curves are generated from simulated potential sweeps (1 V to 0 V in 80 min) with 25 ppm CO in 40%H_2/N_2/O_2. The performance gain from bleeding is markedly greater at 70 °C, the lower temperature. Notice the shape of the two curves representing non-bleeding: the better performance in the upper part of the curve for the lower temperature is almost certainly influenced by the temperature dependence of the adsorption and desorption rate constants (see the preceding discussion on Fig. 10 and the right-hand side of Fig. 9). The same trend is observed in the two cases representing bleeding, but with the crossover of the two curves happening at a much lower cell voltage. The right-hand side of Fig. 13 shows the evolution of CO, H_2 and O_2 coverages for the two cases with bleeding. Recall that a lower temperature leads to lower adsorption and desorption rate constants for H_2 and CO with the decrease in the CO adsorption constant dominating. Moreover, the ratio of O_2 desorption to adsorption rate constant, b^{O}_{ads}, is decreased by an order of magnitude at the lower temperature. We conjecture that this dependence (and that of the protonic conductivity) on temperature influence the result; however, system (25)–(27) is simply too non-linear to unravel with a single example the exact path that leads to the profiles and curves in Fig. 13. Adsorption, desorption, electro-oxidation and heterogeneous catalysis also depend non-linearly on the surface coverages, concentrations and overpotential, which are in turn influenced by other quantities. This point is not pursued further (apart from a brief discussion later) but is worthy of further exploration, preferably in combination with experiment.

4.2. Effects of Pt–Ru alloys

By incorporating the bi-functional mechanism proposed by Watanabe and Motoo [39], in this section we investigate the role of Ru in designing 'CO tolerant' catalyst alloys. Modified versions of this mechanism have previously been employed for PEMFC, most notably by Camara et al. [35] and by Enbäck and Lindbergh [36]. Both cases are restricted to the kinetic problem in the anode, the former including H_2 (at steady-state) and the latter neglecting it (with transient effects included). Here we use the dualistic approach in [36], in which it is assumed that CO adsorbs preferentially onto the Pt sites and water adsorbs preferentially onto the Ru sites, and that the adsorbed OH species are mobile enough to reach the Ru sites where CO is oxidized. It is assumed therefore that the surface electro-oxidation of CO by OH is dependent on the CO coverage on Pt and OH coverage on Ru. It is known that H_2 electro-oxidation on Ru is roughly two orders of magnitude smaller than on Pt [32], and is therefore neglected. Adsorption of water occurs at a significantly lower potential on pure Ru than on Pt [52], and so adsorption on Pt is not included as a simplification. Adsorption of CO on Ru is also considered small in this approximation, as in [36]. Though somewhat simplified, we shall demonstrate that this model captures several salient features and is qualitatively similar to a more complex model that includes CO adsorption and oxidation on Ru.

The (bi-functional) mechanism to be modelled (supplementing (23)) is

$$\text{H}_2\text{O adsorption on Ru}: \quad \text{H}_2\text{O} + \text{M} \rightleftharpoons \text{OH–M} + \text{H}^+ + \text{e}^-,$$

$$\text{CO electro-oxidation by OH on Pt}: \quad \text{CO–M} + \text{OH–M} \rightleftharpoons \text{H}^+ + \text{e}^- + \text{CO}_2 + 2\text{M} \tag{34}$$

In this dualistic approach the already-defined surface coverages are now assumed to be valid on the Pt sites only. The Ru sites are assumed to be occupied by OH, which has surface coverage θ^{Ru}_{OH}, or else free, with surface coverage θ^{Ru}_{M}

$$\theta_{CO} + \theta_H + \theta_M = 1, \qquad \theta^{Ru}_{OH} + \theta^{Ru}_{M} = 1$$

assuming that there is no O_2 present. The equations for the evolution of the coverages of CO (on Pt) and OH (on Ru) are therefore

$$\rho \frac{\mathrm{d}\theta_{CO}}{\mathrm{d}t} = q_{CO,ads} - q_{CO,ox} - q_{CO–OH,ox} \tag{35}$$

$$\rho_{Ru} \frac{\mathrm{d}\theta^{Ru}_{OH}}{\mathrm{d}t} = q_{H_2O,ads} - q_{CO–OH,ox} \tag{36}$$

where the extra terms (arising from (34)) are defined as

$$\begin{aligned} q_{CO–OH,ox} = {} & k_1 \theta^{Ru}_{OH} \theta_{CO}\, \mathrm{e}^{F\eta_a/2RT}\, \mathrm{e}^{\beta r \theta_{CO}/RT}\, \mathrm{e}^{\beta_2 r_2 \theta^{Ru}_{OH}/RT} \\ & - k_{-1} \theta^{Ru}_{M} \theta_M C_{CO_2,e}\, \mathrm{e}^{-F\eta_a/2RT}\, \mathrm{e}^{-(1-\beta) r \theta_{CO}/RT} \\ & \times \mathrm{e}^{-(1-\beta_2) r_2 \theta^{Ru}_{OH}/RT} \end{aligned} \tag{37}$$

and

$$\begin{aligned} q_{H_2O,ads} = {} & k_2 C_d \theta^{Ru}_{M}\, \mathrm{e}^{F\eta_a/2RT}\, \mathrm{e}^{-\beta_2 r_2 \theta^{Ru}_{OH}/RT} \\ & - k_{-2} \theta^{Ru}_{OH}\, \mathrm{e}^{-F\eta_a/2RT}\, e^{(1-\beta_2) r_2 \theta^{Ru}_{OH}/RT} \end{aligned} \tag{38}$$

It is assumed that the adsorption of water on Ru occurs from the dissolved phase, so that the right-hand side of Eq. (8) now contains an extra term in the ACL. Similarly, the ACL terms S_{ϕ_e} and S_{ϕ_s} in Eq. (7) are modified to account for proton and electron generation in (34). Therefore, in Table 2 we now have (for the ACL)

$$\text{RHS of Eq. (8)} = -S_{ad} - S_{dl} - a_{Ru} q_{H_2O,ads},$$

$$S_{\phi_e} = -S_{\phi_s} = aF(q_{H,ox} + 2q_{CO,ox} + q_{CO–OH}) + a_{Ru} F q_{H_2O,ads} \tag{39}$$

Moreover, the active surface area of Pt, a, is now a function of the Pt–Ru ratio, $r_{Pt–Ru}$

$$a = a_T r_{Pt–Ru}, \qquad a_{Ru} = a_T - a$$

where a_T is the combined active surface area of Pt and Ru and a_{Ru} is the surface area of Ru.

The kinetics for H_2O adsorption are based on a Frumkin isotherm, [53], with interaction parameter, r_2, and symmetry coefficient, β_2, both of which were fixed at the values given in [36]. The values of the forward and backward rate constants k_2 and k_{-2} were also based on those in [36] (see Table 6). In order to achieve the correct qualitative trends the parameters k_1 and

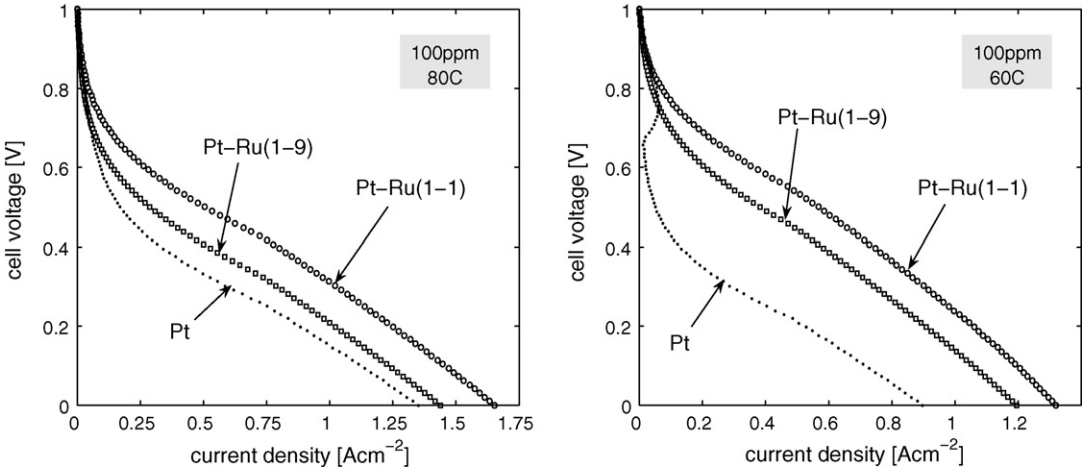

Fig. 14. A demonstration of effects of changes in the ratio of platinum to ruthenium and in the channel temperatures. For a list of the remaining parameters and conditions see Tables 6 and 7.

k_{-1} were adjusted. The selected value of k_1 was much larger than that used in [36], reflecting the competition between CO oxidation and the other mechanisms in (23) and (34), as well as the influence of the transport phenomena. Neither of these were not considered in [36].

Fig. 14 shows the effect of changes in both the ratio of Pt to Ru and in the channel temperatures (other parameters as in Tables 5–7). These are again simulations of potential sweeps from 1 to 0 V in 80 min. The best performance is seen for a Pt–Ru ratio of 1–1 and the worst for pure Pt, with the performance for a Pt–Ru ratio of 1–9 intermediate between these two case, at both temperatures. The use of Pt–Ru involves a trade-off between increased CO electro-oxidation (by the OH species) occurring at low potentials on the Ru, and decreased H_2 oxidation on the Ru portion of the catalyst surface, implying that there is an optimal ratio of Pt to Ru surface area (or volume) at which the best performance on reformate is achieved. This result is in agreement with the experiments in [54] (and references therein), where the authors concluded an optimal Pt–Ru ratio of between 1–1 and 1–3. Moreover, it supports the applicability of the bifunctional mechanism (34). The results shown in Fig. 14 suggest that at elevated temperatures the effect of Ru on the performance is less visible, matching the conclusion in [54]. The reasons for this will include the temperature effect on membrane conductivity and on CO adsorption and desorption already encountered in Fig. 9.

Adsorption of CO on Ru was neglected in the model above. Assuming that adsorption and oxidation can be modelled with Eq. (26), i.e. the following equation for CO on Ru is added to (35):

$$\rho_{\mathrm{Ru}}\frac{\mathrm{d}\theta_{\mathrm{CO}}^{\mathrm{Ru}}}{\mathrm{d}t} = k_{\mathrm{ads}}^{\mathrm{CO}}\,\mathrm{e}^{-\beta r\theta_{\mathrm{CO}}^{\mathrm{Ru}}/RT}(C_{\mathrm{CO,e}}\theta_{\mathrm{M}}^{\mathrm{Ru}} - b_{\mathrm{ads}}^{\mathrm{CO}}\theta_{\mathrm{CO}}^{\mathrm{Ru}}\,\mathrm{e}^{r\theta_{\mathrm{CO}}^{\mathrm{Ru}}/RT}) - 2k_{\mathrm{ox}}^{\mathrm{CO}}\theta_{\mathrm{CO}}\,\sinh\left(\frac{F\eta_{\mathrm{a}}}{2RT}\right) \quad (40)$$

the results are qualitatively the same if the rate constants are adjusted. In Fig. 15 the results at 60 °C in Fig. 14 are

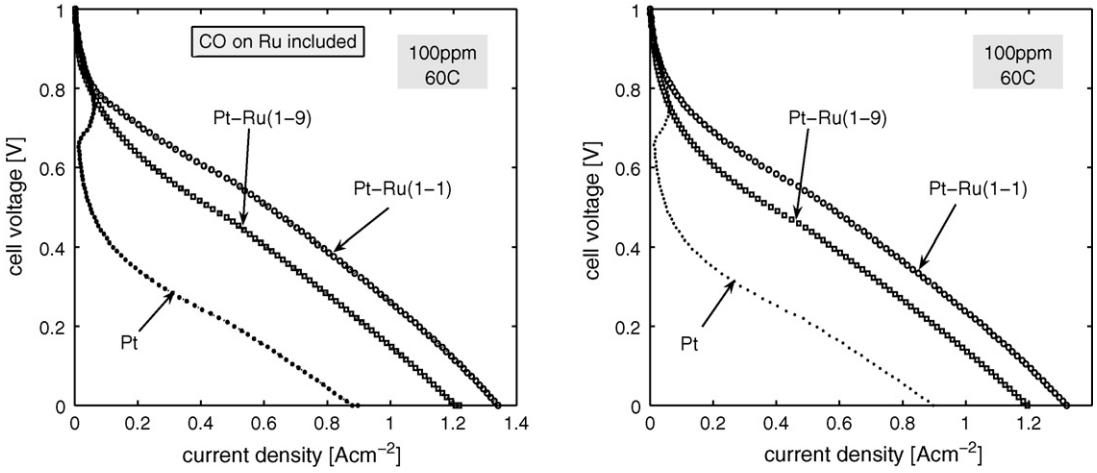

Fig. 15. A comparison of the models with CO adsorption and oxidation on Ru included (left-hand side) and neglected (right-hand side).

compared with a model that includes Eq. (40). The rate constants were fitted as $k_1 = 2.5 \times 10^{-6}$ mol m^{-2} s^{-1} and $k_2 = 1 \times 10^{-5}$ mol m^{-2} s^{-1} (the other constants as in Table 6), which are much larger than the values in Table 6 since the H_2O now competes with CO for adsorption onto Ru.

5. Conclusions

CO poisoning and O_2 bleeding in PEMFC are largely influenced by the (rates of) the electrochemical reactions in the anode. However, neglecting other important effects reduces the number of realistic settings that we can hope to simulate with modelling; these effects can influence and also be influenced by the kinetics. This point is amply illustrated in the examples provided, such as Figs. 7 and 8 and the associated discussion; excluding liquid-water transport and membrane hydration can result in conclusions that hold true only in the most idealized of settings. In the general case PEMFC operation is the conflation of several competing processes, and if a model is to be used as a predictive or diagnostic tool inclusion of these fundamental phenomena is likely to be necessary.

Equally as important for automobile applications (in particular) is that steady-state modelling of CO poisoning provides incomplete, and perhaps misleading information. In, for example, the right-hand side of Fig. 9 and the left-hand side of Fig. 13 we see that evaluating the response of the system on a long time scale can mask shorter term features that are of potential significance for real events that can last for seconds, minutes or even a few hours. The results contained in these examples, demonstrating the effects of temperature on the transient response, could have far-reaching implications if verified by experiment.

The parameter space of possible investigation is extremely high dimensional, reflecting the many physical properties and external influences that can be important in the phenomenology. In the current model Tables 5–7 list about 75, many of which take a value specific to a particular physical configuration or material. Enumeration of all possibilities is therefore impracticable. The primary objective has been to demonstrate the flexibility in the framework and its ability to capture, predict and possibly explain the complex interactions observed in experiment. Natural techniques to investigate the short- and long-term effects of CO poisoning and O_2 bleeding include cyclic voltammetry, as in [49], and the pulsing experiments found in [50,51]. In principle, such experiments are less time-consuming than steady-state alternatives, and are more applicable to PEM fuel cell operation in many if not most applications. The modelling tool we have outlined in this paper is an ideal accompaniment for such experiments, to help reduce the number (and therefore cost) of laboratory investigations, and to help understand the results.

Of course, there are several stages in reaching such an outcome. There remains some uncertainty in the (electro) chemical rate constants (29). A great deal more transient data is required to estimate or fit these parameters in as wide a range of parameter space as possible, including investigations into the effects of sweep rate, temperature, anode pressure and water activity. Characterization of the electrochemistry for Pt alloys (other than Pt–Ru) currently in use would also be of extreme benefit. These avenues, along with a confirmation of the widely occurring behaviour demonstrated in Figs. 9 and 13, represent practical complements to the present work.

Acknowledgment

The authors are grateful to Ballard Power Systems Inc. for funding contributing to the present and ongoing research.

References

[1] J. Cao, N. Djilali, Proceedings of the 10th Canadian Hydrogen Conference, 2000, pp. 447–456.
[2] W. He, J. Yi, T.V. Nguyen, AIChE J. 46 (10) (2000) 2053–2064.
[3] G. Lin, W. He, T. Van, Nguyen, J. Electrochem. Soc. 151 (12) (2004) A1999–A2006.
[4] S. Mazumder, J.V. Cole, J. Electrochem. Soc. 150 (11) (2004) A1510–A1517.
[5] D. Natarajan, T.V. Nguyen, J. Electrochem. Soc. 148 (12) (2001) A1324–A1335.
[6] N.P. Siegel, M.W. Ellis, D.J. Nelson, M.R. von Spakovsky, J. Power Sources 115 (2003) 81–89.
[7] N.P. Siegel, M.W. Ellis, D.J. Nelson, M.R. von Spakovsky, J. Power Sources 128 (1) (2004) 173–184.
[8] L.B. Wang, N.I. Wakayama, T. Okada, Chem. Eng. Sci. 60 (2005) 4453–4467.
[9] Z.H. Wang, C.-Y. Wang, K.S. Chen, J. Power Sources 94 (2001) 40–50.
[10] H. Meng, C.-Y. Wang, J. Electrochem. Soc. 152 (9) (2005) A1733–A1741.
[11] U. Pasaogullari, C.-Y. Wang, J. Electrochem. Soc. 152 (2) (2005) A380–A390.
[12] L. You, H. Liu, J. Power Sources 155 (2006) 219–230.
[13] H. Ju, H. Meng, C.-Y. Wang, Int. J. Heat Mass Transfer 148 (7) (2005) 1303–1315.
[14] C.-Y. Wang, Chem. Rev. 104 (2004) 4727–4766.
[15] A.Z. Weber, J. Newman, Chem. Rev 104 (2004) 4679–4726.
[16] S. Um, C.-Y. Wang, K.S. Chen, J. Electrochem. Soc. 147 (12) (2000) A4485–A4493.
[17] S. Um, J. Power Sources 156 (2006) 211–223.
[18] A. Vath, Z. Lěmes, H. Mäncher, M. Sohn, N. Nicoloso, T. Hartkopf, J. Power Sources 157 (2006) 816–827.
[19] S. Shimpalee, W.K. Lee, J.W. Van-Zee, H. Naseri-Neshat, J. Power Sources 156 (2006) 355–368.
[20] C.-Y. Wang, P. Cheng, J. Power Sources 30 (1997) 93–196.
[21] Y. Wang, C.-Y. Wang, Electrochim. Acta 51 (2006) 3924–3933.
[22] C. Ziegler, H.M. Yu, J.O. Schumacher, J. Electrochem. Soc. 152 (8) (2005) A1555–A1567.
[23] A.A. Shah, G.S. Kim, P.C. Sui, D. Harvey, J. Power Sources 163 (2) (2007) 793–806.
[24] V.O. Mittal, H.R. Kunz, J.M. Fenton, Electrochem. Solid-State Lett. 9 (6) (2006) A299–A302.
[25] T.E. Springer, T. Rockward, T.A. Zawodinski, S. Gottesfeld, J. Elecrochem. Soc. 148 (1) (2001) A11–A23.
[26] J.J. Baschuk, X. Li, Int. J. Ener. Res. 25 (2001) 695–713.
[27] J.J. Baschuk, A.M. Rowe, X. Li, J. Ener. Res. Technol. 125 (2003) 94–100.
[28] J.J. Baschuk, X. Li, Int. J. Ener. Res. 27 (2003) 1095–1116.
[29] K.K. Bhatia, C.-Y. Wang, Electrochim. Acta 49 (2004) 2333–2341.
[30] S. Jimenez, J. Soler, R.X. Valenzuela, L. Daza, J. Power Sources 151 (2005) 69–73.
[31] J.S. Gottesfeld, J. Pafford, J. Electrochem. Soc. 135 (10) (1988) 2651–2652.
[32] H.A. Gasteiger, N. Markovic, P.N. Ross, E.J. Cairns, J. Electrochem. Soc. 141 (7) (1994) A1795–A1803.
[33] T. Zhou, H. Liu, J. Power Sources 138 (2004) 101–110.
[34] H.S. Chu, C.P. Wang, W.C. Liao, W.M. Yan, J. Power Sources 159 (2006) 1071–1077.

[35] G.A. Camara, T.A. Ticianelli, S. Mukerjee, S.J. Lee, J. McBreen, J. Electrochem. Soc. 149 (6) (2002) A748–A753.
[36] S. Enback, G. Lindbergh, J. Electrochem. Soc. 152 (1) (2005) A23–A31.
[37] D.B. Genevey, Master's Thesis, Virginia Polytechnic Institute, 2004.
[38] Y. Wang, C.-Y. Wang, Electrochim. Acta 50 (2005) 1307–1315.
[39] M. Watanabe, S. Motoo, J. Electroanal. Chem. 60 (1975) 275–283.
[40] B. Bird, W. Stewart, E. Lightfoot, Transport Phenomena, John Wiley and Sons, 2002.
[41] J-H. Nam, M. Kaviany, Int. J. Heat Mass Trans. 46 (2003) 4595–4611.
[42] J.T. Hinatsu, M. Mizuhata, H. Takenaka, J. Elecrochem. Soc. 141 (1994) A1493–A1497.
[43] S. Ge, X. Li, B. Yi, I.M. Hsing, J. Electrochem. Soc. 152 (6) (2005) A1149–A1157.
[44] J. Zhang, T. Thampan, R. Datta, J. Electrochem. Soc. 6 (149) (2002) A765–A772.
[45] A.W. Adamson, Physical Chemistry of Surfaces, Interscience, New York, 1967.
[46] E. Gileadi, E. Kirowa-Eisner, J. Penciner, Interfacial Electrochemistry An Experimental Approach, Addison-Wesley Publishing Company, Reading, MA, 1975.
[47] T.E. Springer, T.A. Zawodinski, S. Gottesfeld, J. Elecrochem. Soc. 138 (8) (1991) A2334–A2341.
[48] X.G. Yang, F.Y. Zhang, A.L. Lubawy, C.-Y. Wang, Electrochem. Solid-State Lett. 7 (11) (2004) A408–A411.
[49] H.M. Yu, C. Ziegler, J. Electrochem. Soc. 153 (3) (2006) A570–A575.
[50] M. Murthy, M. Esayian, A. Hobson, S. MacKenzie, W.-K. Lee, J.W. Van-Zee, J. Electrochem. Soc. 148 (10) (2001) A1141–A1147.
[51] M. Murthy, M. Esayian, W.-K. Lee, J.W. Van-Zee, J. Electrochem. Soc. 150 (1) (2003) A29–A34.
[52] H.A. Gasteiger, N. Markovic, P.N. Ross, E.J. Cairns, J. Phys. Chem. 99 (1995) 16757–16767.
[53] J.O'M. Bockris, S.U.M. Khan, Surface Chemistry, A Molecular Level Approach, Plenum Press, 1993.
[54] E. Antolini, L. Giorgi, F. Cardellini, E. Passalacqua, J. Solid State Electrochem. 5 (2001) 131–140.
[55] S. Lister, G. McLean, J. Power Sources 130 (2004) 61–76.
[56] M.V. Williams, H.R. Kunz, J.M. Fenton, J. Elecrochem. Soc. 151 (10) (2004) A1617–A1627.
[57] T. Van Nguyen, W. He, in: W. Vielstich, A. Lamm, H. Gasteiger (Eds.), Handbook of Fuel Cells—Fundamentals, Technology and Applications, vol. 3, John Wiley & Sons, 2003 (Chapter 46).
[58] U. Pasaogullari, C.-Y. Wang, K.S. Chen, J. Electrochem. Soc. 152 (8) (2005) A1574–A1582.
[59] M.J. Lampinen, M. Fomino, J. Electrochem. Soc. 140 (12) (1993) A3537–A3546.
[60] S. Motupally, A.J. Becker, J.W. Weidner, J. Electrochem. Soc. 147 (9) (2000) A3171–A3177.
[61] Z. Ogumi, Z. Takehara, S. Yoshizawa, J. Electrochem. Soc. 131 (4) (1984) A769–A772.
[62] C.R. Wilke, P. Chang, AIChE J. 1 (2) (1955) 264–270.
[63] Suk Won Cha, PhD Thesis, Stanford University, 2003.
[64] C. Ziegler, A. Schmitz, M. Tranitz, E. Fontes, J.O. Schumacher, J. Electrochem. Soc. 151 (12) (2004) A2028–A2041.
[65] W. Sun, B.A. Peppley, K. Karan, Electrochim. Acta 50 (2005) 3359–3374.
[66] N.P. Siegel, PhD Thesis, Virginia Polytechnic Institute, 2003.